First year report

Measurements of Aerosol Refractive Index: A New Refractometer Method

Benjamin E. Reed

Supervisor: Don Grainger

Postdoctoral advisor: Dan Peters

September 2012

Contents

1 Overview **3**

2 Aerosols **4**
2.1 Introduction to Aerosols 4
2.2 The influence of aerosols on the atmosphere 4
2.2.1 Radiative influence of aerosols 4
2.2.2 The influence of aerosols on clouds 5
2.2.3 Chemical influence 6

3 Theory **8**
3.1 The Maxwell equations of continuum electrodynamincs 8
3.1.1 Microscopic fields 8
3.1.2 Macroscopic fields 9
3.1.3 Boundary conditions 9
3.2 Important optical quantities 9
3.2.1 Complex refractive index 9
3.2.2 Size parameter 10
3.2.3 The scattering matrix 11
3.2.4 Cross-sections and efficiency factors 12
3.2.5 Single scatter albedo 12
3.2.6 The phase function 12
3.3 Mie theory 13
3.3.1 Method of derivation 13
3.3.2 Mie amplitude functions 13
3.3.3 Mie efficiency factors 14
3.3.4 Mie scattering code 14
3.4 The concept of an effective refractive index for a slab of many scatterers . . . 15
3.4.1 The fundamental extinction formula 15
3.4.2 A slab of many scatterers 16
3.5 The Fresnel equations 17

4 A new refractometer method **19**
4.1 Introduction 19
4.2 CSM theory 20
4.3 The relationship between sensitivity to refractive index and particle radius . . 22

4.4 The apparatus and experimental set up . . . 24
4.4.1 Laser power stability . . . 26
4.4.2 Angular arm positions . . . 27
4.5 Validating the experimental set up and CSM theory . . . 28
4.5.1 Introduction to the general method . . . 28
4.5.2 Error propagation . . . 30
4.5.3 Glass and water measurements - Fresnel reflectance . . . 31
4.5.4 Polystyrene spherical latex beads - CSM . . . 33
4.5.5 Application of CSM to 'ash-like' commercial sand . . . 37

5 The Becke line method 41
5.1 Introduction . . . 41
5.2 Experimental method . . . 42
5.2.1 Wavelength dependence and coefficient of variation with temperature of the refractive index liquids . . . 42
5.2.2 Sample preparation . . . 42
5.2.3 Optimal microscope set up for viewing the Becke line . . . 42
5.2.4 Particle sizing . . . 43
5.2.5 Becke line method for an aerosol sample . . . 43
5.3 Results and Analysis . . . 46
5.3.1 Particle Size Range . . . 46
5.3.2 Sample refractive index results and analysis . . . 46

6 Conclusions and future work 49
6.1 Conclusions . . . 49
6.2 Plan for future work . . . 49
6.2.1 Further work with the CSM refractometer . . . 49
6.2.2 Work on SPARCLE . . . 50
6.3 Transferable skills . . . 51

Chapter 1

Overview

The principle focus of my work this year has been on the development of a new refractometer device for measuring aerosol refractive indices in the visible. The device makes use of a coherent scattering model (CSM) to infer aerosol optical properties — principally the real part of the particle refractive index — from laser reflectivity measurements about an interface with a turbid suspension containing the particles. The device employs a laser diode of wavelength 635 nm and so the refractive indices measured are valid at this wavelength.

In addition to this, in order to provide an independent check of the refractometer measurements, microscopic Becke line tests were performed on a range of aerosol samples.

The measurements made this year and the development of the refractometer device are very much relevant with regard to the wider context of my thesis. In the near future, I will begin work on the further development of SPARCLE, an advanced Optical Particle Counter (OPC). The device has the potential to measure, on a particle by particle basis, both particle size and refractive index simultaneously — a unique concept in aerosol measurement. The measurements of refractive index already made as well as future measurements with the refractometer will therefore provide an invaluable check of results derived from SPARCLE. It is hoped the methods developed this year and the future work on SPARCLE will provide a comprehensive suite of techniques for the measurement of aerosol optical properties.

Chapter 2.1 of this report gives a background to the subject of aerosols, in particular aiming to illuminate the importance of measuring aerosol optical properties.

In Chapter 3 the main theoretical concepts relevant to the refractometer device are presented — chiefly the scattering theory of aerosol particles is summarised. These concepts will also be highly relevant for future work on the development of SPARCLE.

The work performed on the development of the refractometer device is presented in Chapter 4. A validation of the apparatus and experimental method is summarised. The results for measurements performed on test particles with known physical properties are given. The results provide a validation of the coherent scattering model (CSM) used as the forward model for the retrieval of aerosol refractive index from the refractometer measurements.

The Becke line method and the results of the tests performed are presented in Chapter 5, along with a discussion of the implications of these results.

The final chapter summarises the main conclusions that can be drawn from the results, and also compares the two techniques that have been used. A plan for future work is also presented here.

Chapter 2

Aerosols

2.1 Introduction to Aerosols

As defined in the simplest sense, an aerosol is a two-phase system consisting of solid or liquid particles and a gas in which these particles are suspended. Aerosol particles in the amtmosphere have a range of sizes from just a few molecules up to diameters larger than 100μm. These particles have a wide variety of sources and vary greatly in their physical and chemical properties, resulting in great variability in their influence on the atmosphere. As well as the aerosol sources, the atmospheric aerosol content at any give time is determined by the removal mechanisms. The primary removal mechanisms are sedimentation and rain washout.

Broadly speaking aerosol sources can be split into two main groups: natural sources — such as wind-driven sand uptake and volcanic emissions; or anthropogenic sources — for example black carbon emission from incomplete combustion processes.

Primary aerosol consists of aerosols emitted directly into the atmosphere. Secondary aerosol consists of particles that have been formed in the atmosphere by a gas-to-particle conversion process.

The main sources of aerosol emissions are: 1) aerosol from fossil fuel combustion in populated urban and industrial regions, 2) aerosol produced from biomass burning in grassland and forest fires, 3) wind-driven dust uptake from desert regions, and 4) marine aerosol (primarily salt). Each aerosol group differs in their physical properties and therefore their influence on the atmosphere.

2.2 The influence of aerosols on the atmosphere

2.2.1 Radiative influence of aerosols

The interaction of aerosols with radiation is greatest when the aerosol dimensions are similar to the radiation wavelength, i.e. when the size parameter $x \sim 1$. Longer lived aerosols in the accumulation mode (0.1–1.0 μm) therefore effect short-wave solar radiation more significantly than the long-wave infra-red radiation emitted by the atmosphere and the earth's surface. Understanding the radiative effect of aerosols requires an understanding of scattering theory, which will be discussed in detail in Chapter 3.

Radiative forcing (RF) is defined[1] as the change in net (downward minus upward) irradiance (solar plus longwave; with units W m^{-2}) at the tropopause. The concept of RF provides a useful measure of the relative impact of a certain factor on climate change. The important parameters for determining aerosol RF are aerosol optical properties, for example the single scattering albedo, $\tilde{\omega}_0$, the extinction cross section, C_{ext}, and the scattering phase function, P, all of which depend on the physical properties of the particles — complex refractive index, shape and size (see §3.2). Early studiese, for example *Ramaswamy et al.* [2001], on long-lived greenhouse gases (LLGHGs) assumed a linear response to RF in global mean equilibrium surface temperature change, i.e. $\Delta T_S = \lambda RF$. Modelling the climate response to pertrubations in RF is significantly complicated by uncertainties quantifying climate sensitivity and feedback processes [*Solomon et al.*, 2007].

Figure 2.1, taken from the IPCC Fourth Assessment Report [*Solomon et al.*, 2007], shows estimated values of RF, with associated uncertainties, for various anthropogenic and natural effects. It can be seen that uncertainties in aerosol properties give rise to one of the largest uncertainties in atmospheric radiative forcing — thereby limiting our best predictions of future climate change

In Figure 2.1 the aerosol effect has been split into contributions from the direct effect and the indirect effect (or cloud albedo effect). It can be seen that the uncertainty ranges for these are the largest for any factor, and the level of understanding is described as 'medium-low' for the direct effect and 'low' for the indirect effect. The indirect effect refers to the influence of aerosols on clouds, and will be discussed in the next section.

The main reason for the low levels of understanding associated with the aerosol direct effect comes from a lack of detailed knowledge of aerosol optical properties. Additionally, monitoring aerosol atmospheric content is difficult. Compared to greenhouse gases, where the uncertainties in RF are lowest, atmospheric aerosol content is highly inhomogeneous and variable. This is demonstrated by Figure 2.2, which shows global and seasonal variation in total aerosol optical depth for mid-visible wavelengths.

2.2.2 The influence of aerosols on clouds

Aerosols play and important role in the formation of clouds by providing cloud condensation nuclei (CCN), and also by influencing the microphysical properties of clouds. Clouds, due to their high reflectivity of solar radiation, have a large affect on the Earth's albedo, and therefore changes in cloud propeties brought about by varying atmospheric aerosol content will affect atmospheric RF. This is referred to as the aerosol indirect effect. The understanding of the complexities of this effect is by no means complete, and this gives rise to one of the largest uncertainties in RF seen in Figure 2.1.

There are several mechanisms by which aerosol content influences cloud properties. Firstly — the so called Twomey effect [*Twomey*, 1977] — an increase in aerosol particulates, for a fixed total cloud water content, leads to an increase in the number of water droplets in the

[1]The IPCC Fourth Assessment Report uses the definition of *Ramaswamy et al.* [2001] as 'the change in net irradiance at the tropopause after allowing for stratospheric temperatures to readjust to radiative equilibrium, but with surface and tropospheric temperatures and state held fixed at the unperturbed values' although others define it as the top of atmosphere perturbation. In any case, for aerosols the stratospheric adjustment makes little difference.

Figure 2.1: Average global RF estimates and uncertainty ranges in 2005. Taken from the IPCC Fourth Assessment Report 2007: Working Group 1. LOSU is the level of scientific understanding.

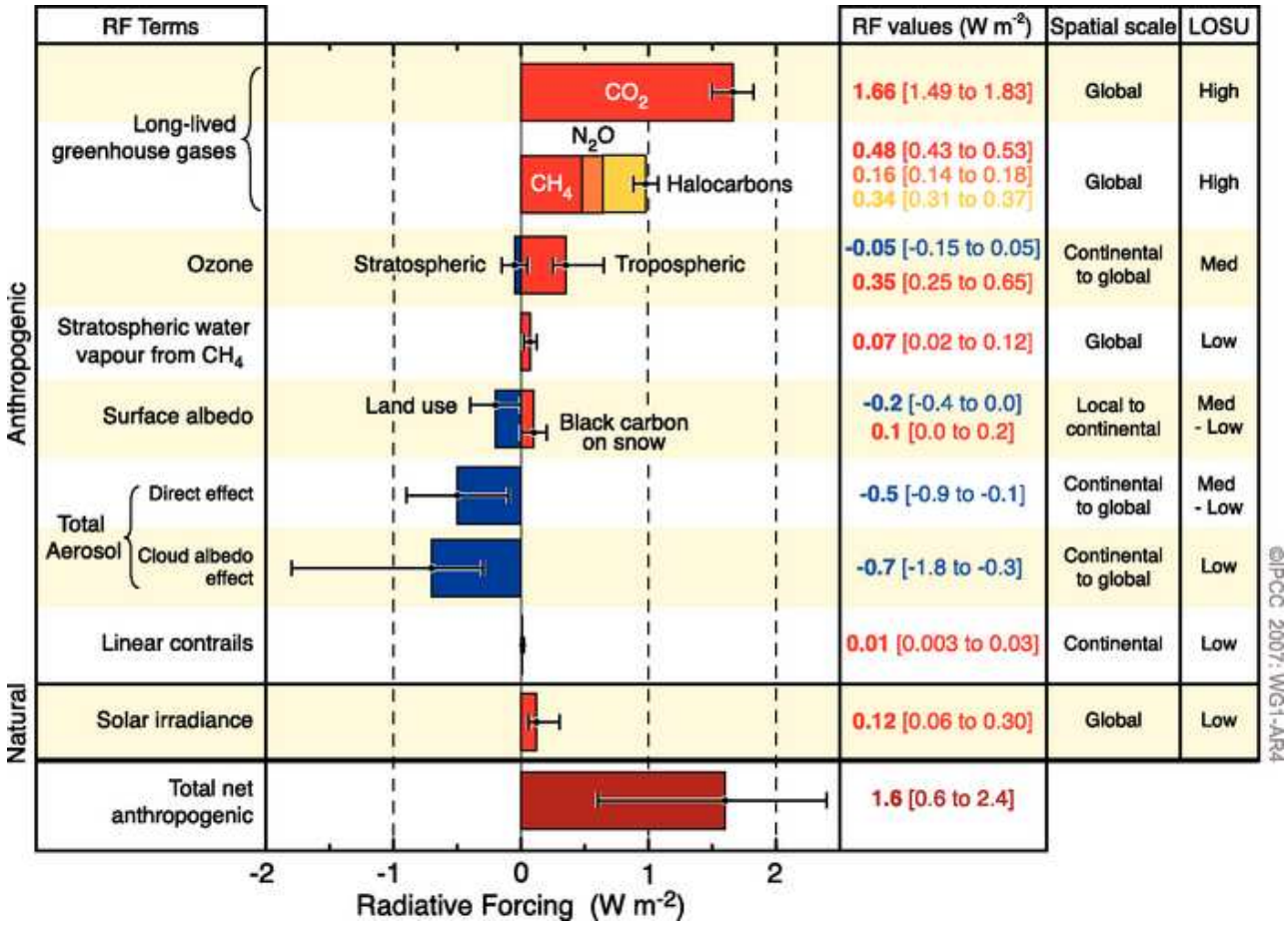

cloud, but with a corresponding decrease in droplet radius. The result is an increase in the total surface area of droplets in the cloud, and therefore an increase in the reflectivity of the cloud. Secondly — the Albracht effect — increased aerosol content can lead to an increase in the water content and lifetime of clouds by suppressing drizzle [*Albrecht*, 1989; *Rosenfeld*, 2006].

2.2.3 Chemical influence

Aerosols are involved in heterogeneous reactions. A heterogeneous reaction is one that involves a reaction between substances in different phases — liquid or solid aerosols may react directly with atmospheric gas molecules, or may act as a catalyst providing an activation surface for a reaction.

An important example is the reaction between chlorine nitrate and hydrochloric acid on the surface of aerosol particles in stratospheric clouds. The resultant molecular chlorine is photolyzed to produce chlorine radicals which play an important role in the ozone depletion cycle [*Bianco and Hynes*, 2006].

Figure 2.2: Global variation and seasonal variation in total aerosol optical depth at mid-visible wavelengths as determined by satellite measurements. Source: *Solomon et al.* [2007]

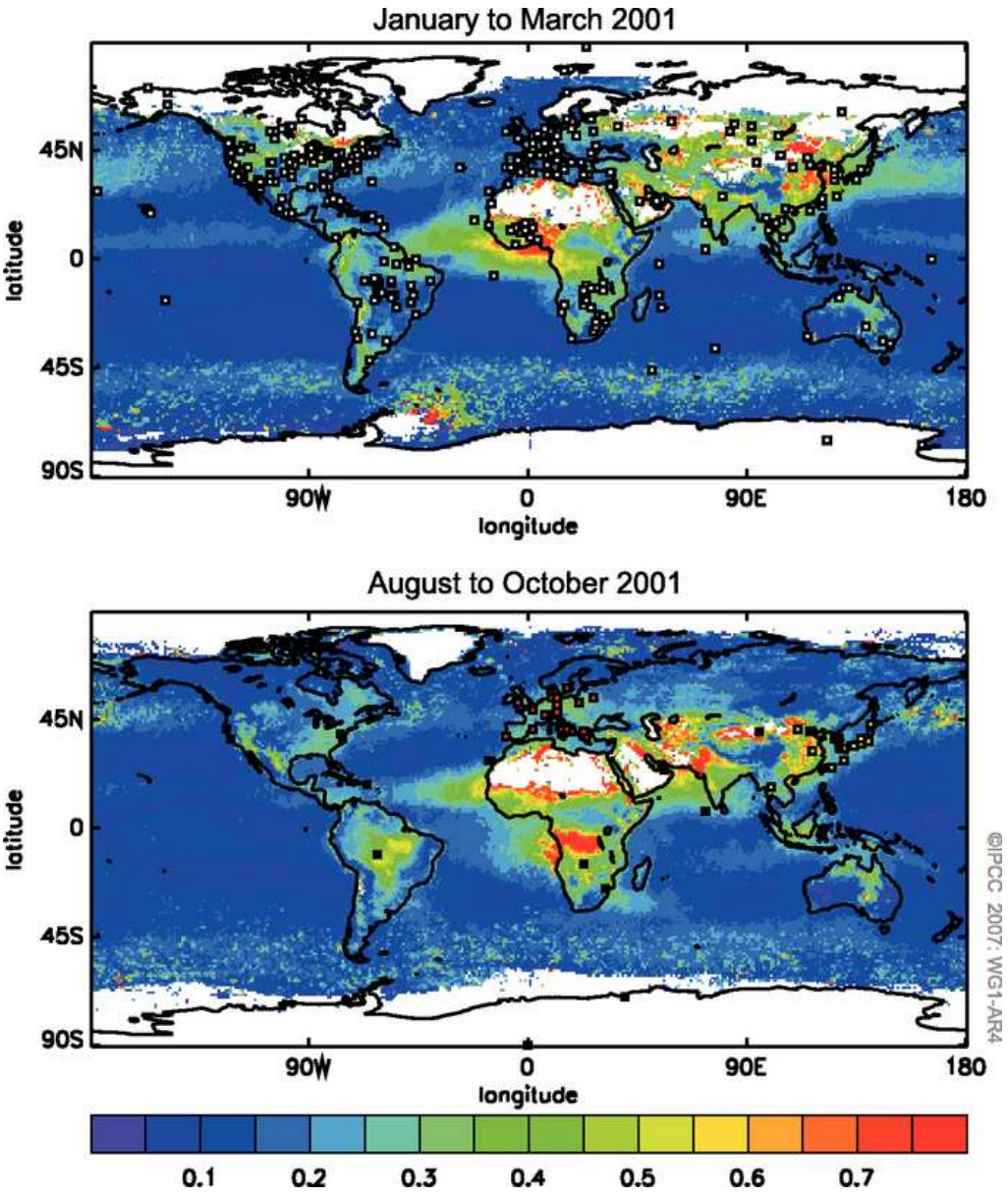

Chapter 3

Theory

3.1 The Maxwell equations of continuum electrodynamincs

3.1.1 Microscopic fields

The Maxwell equations for the microscopic electromagnetic field in a material with a continuous electric permitivity ϵ and magnetic permeability μ, containing charge density ρ and with a current density $\mathbf{J}$ can be expressed as:

$$\nabla \cdot \mathbf{E} = \frac{\rho}{\epsilon} \tag{3.1}$$

$$\nabla \wedge \mathbf{E} = -\frac{\partial \mathbf{B}}{\partial t} \tag{3.2}$$

$$\nabla \cdot \mathbf{B} = 0 \tag{3.3}$$

$$\nabla \wedge \mathbf{B} = \mu\mathbf{J} + \mu\epsilon\frac{\partial \mathbf{E}}{\partial t} \tag{3.4}$$

The propagation of light can be described as the plane wave solution to these differential equations. For light propagating in the vacuum we have $\rho = 0$ and $\mathbf{J} = 0$. Then taking the curl of equation 3.2 and combining with equation 3.4 yields:

$$\nabla^2\mathbf{E} = \mu\epsilon\frac{\partial^2 \mathbf{E}}{\partial t^2} \tag{3.5}$$

Similarly an identical wave equation for $\mathbf{B}$ can be derived. The plane wave solution for an electromagnetic wave propagating in the positive z direction has the form:

$$\mathbf{E} = \mathbf{E}_i \exp(ikz - i\omega t); \quad \mathbf{E}_i = E_\parallel \hat{\mathbf{e}_\parallel} + E_\perp \hat{\mathbf{e}_\perp} \tag{3.6}$$

It is worth noting here that mathematically the form $\exp(i\omega t - ikz)$ also describes a wave propagating in the positive z direction. The convention chosen uniquely determines the form of the complex refractive index, a point that will be returned to in section 3.2.1.

It is immediately apparent from properties of the general wave equation and comparison with equation 3.20 that the phase velocity, $v_p = \frac{\omega}{k}$, and group velocity, $v_g = \frac{d\omega}{dk}$, are given by:

$$v_p = v_g = \frac{\omega}{k} = \frac{d\omega}{dk} = \frac{1}{\sqrt{\mu\epsilon}} \tag{3.7}$$

3.1.2 Macroscopic fields

In electromagnetism it proves useful to define the auxiliary fields $\mathbf{H}$ and $\mathbf{D}$, so that the Maxwell equations do not depend on bound charge and current, and only depend on free charge and currents:

$$\mathbf{D} = \epsilon_0 \mathbf{E} + \mathbf{P} \tag{3.8}$$

$$\mathbf{B} = \mu_0(\mathbf{H} + \mathbf{M}) \tag{3.9}$$

where $\mathbf{P}$ and $\mathbf{M}$ are the polarisation and magnetisation of the material respectively. Bound charge, σ_b, and bound current density, $\mathbf{J}_b$, are defined according to:

$$\sigma_b = -\nabla \cdot \mathbf{P} \tag{3.10}$$

$$\mathbf{J}_b = \nabla \wedge \mathbf{M} + \frac{\partial \mathbf{P}}{\partial t} \tag{3.11}$$

The total charge density is the sum of the free charge density and the bound charge density, and similarly for the total current density:

$$\sigma = \sigma_b + \sigma_f \tag{3.12}$$

$$\mathbf{J} = \mathbf{J}_b + \mathbf{J}_f \tag{3.13}$$

3.1.3 Boundary conditions

At the boundary between two media, from the macroscopic perspective, there is a discontinuity in ϵ and μ (although on the atomic scale there is a gradual transition region). It can be shown that at such a boundary surface S, in the absence of any sources or sinks of electromagnetic energy, conservation of energy requires:

$$[\mathbf{E}_2(\mathbf{x}) - \mathbf{E}_1(\mathbf{x})] \wedge \hat{\mathbf{n}} = 0 \tag{3.14}$$

$$[\mathbf{H}_2(\mathbf{x}) - \mathbf{H}_1(\mathbf{x})] \wedge \hat{\mathbf{n}} = 0 \tag{3.15}$$

where $\hat{\mathbf{n}}$ is the outward normal to the surface S and $\mathbf{x}$ is any point on S. Thus the boundary conditions require that the tangential components of $\mathbf{E}$ and $\mathbf{H}$ are continuous across a boundary.

3.2 Important optical quantities

3.2.1 Complex refractive index

The real part of the refractive index of a material is defined as the ratio of the speed of light in vacuum to the speed of propagation in the material, i.e.

$$n = \frac{c}{v} = \sqrt{\frac{\mu\epsilon}{\mu_0\epsilon_0}} \tag{3.16}$$

Now defining $k_m = 2\pi/\lambda_m$ as the real part of the wavevector in the medium with propagation speed $v = \lambda_m\nu$, and $k_0 = 2\pi/\lambda_0$ as the value in the vacuum, it is straightforward to show that:

$$k_m = \frac{2\pi n}{\lambda_0} \tag{3.17}$$

The complex refractive index is defined by:

$$\tilde{m} = n + i\kappa \tag{3.18}$$

and the corresponding complex wavevector is given by:

$$\tilde{k}_m = \frac{2\pi\tilde{m}}{\lambda_0} \tag{3.19}$$

The complex refractive index of a material is defined so as to encapsulate two effects of the material on a propagating electromagnetic wave: 1) The real part n determines the change in phase speed 2) The imaginary part κ describes the absorption of wave energy.

The imaginary part κ is called the extinction coefficient and it is a positive number for an absorbing medium. Substitution of equation 3.18 into 3.20 making use of equation 3.17 demonstrates the effect of κ as giving exponential decay of the wave amplitude:

$$\mathbf{E} = \mathbf{E}_i e^{-2\pi\kappa z/\lambda_0} e^{(i2\pi nz/\lambda_0 - i\omega t)} \tag{3.20}$$

Note here that for an incident wave of the form $\exp(i\omega t - ikz)$, the appropriate definition of the complex refractive index is $\tilde{m} = n - i\kappa$, so that a positive value of κ gives rise to exponential decay rather than growth.

3.2.2 Size parameter

In scattering theory the size of a particle relative to the incident light is of utmost importance. If the wavelength of light, λ, is very large relative to the particle size then the scattering of light will be negligible. For wavelengths comparable to particle size, the effect of scattering is most significant. The size parameter, x, is dimensionless and defined so as to give a clear measure of the relative size regime of a particle:

$$x = \frac{2\pi a}{\lambda} \tag{3.21}$$

Here a is the particle radius. For non-spherical particles the choice of a is less clear. One definition, used by Mishenko & Travis [1998], takes a to be the radius of an equivalent spherical particle with the same total volume.

Figure 3.1 demonstrates the various scattering regimes. For x less than approximately 0.002 the effect of scattering is negligible, and for $x > 2000$ classical geometric optics apply. In the intermediate region, $2000 > x > 0.002$, the rigorous treatment of Mie Theory is required and will be discussed in Section 3.3. The expressions of Mie Theory involving infinite series reduce,

Figure 3.1: The various size regimes.

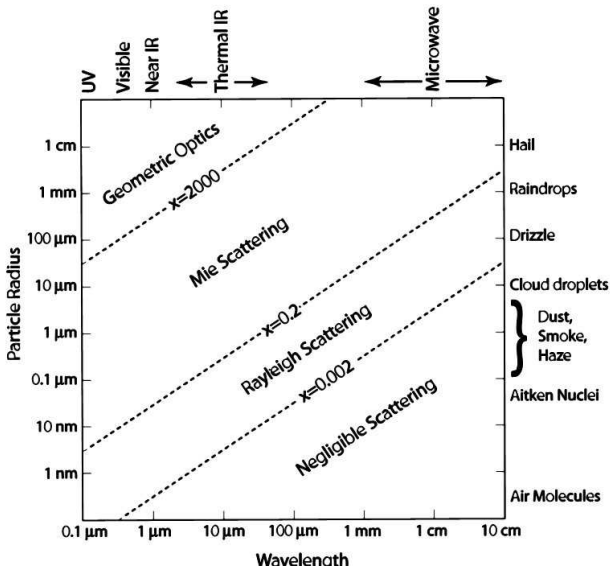

in the limit where x is small, to the simplified formula of Rayleigh scattering. The region of validity of Rayleigh scattering is demonstrated in the figure.

3.2.3 The scattering matrix

Consider the general case of a particle fixed at the origin of arbitrary shape illuminated by a plane wave propagating from the negative z direction (as described by equation 3.20). The scattered wave $\mathbf{E}_s$ in the distant field is a spherical outgoing wave inversely proportional to the distance l from the particle:

$$\mathbf{E}_s = \frac{e^{ik(l-z)}}{-ikl}\mathbf{S}\mathbf{E}_i \tag{3.22}$$

$$\begin{pmatrix} E_{\parallel s} \\ E_{\perp s} \end{pmatrix} = \frac{e^{ik(l-z)}}{-ikl} \begin{pmatrix} S_2 & S_3 \\ S_4 & S_1 \end{pmatrix} \begin{pmatrix} E_{\parallel i} \\ E_{\perp i} \end{pmatrix} \tag{3.23}$$

Note that the definition of *Bohren and Huffman* [1983] has been adopted here, but definitions vary slightly between texts. For example *van der Hulst* [1957] uses the prefactor $e^{-ik(l-z)}/ikl$, i.e. the complex conjugate of that used above, and Mischenko et al. [2000] multiplies by k. In general for a non-spherical particle S_i $(i = 1, 2, 3, 4)$ depend on the scattering angle, θ, and the azimuthal angle, ϕ.

The amplitude functions, S_i, are in general complex, and so may be written as:

$$S_i(\theta, \phi) = s_i \cdot e^{i\sigma_i} \tag{3.24}$$

where s_i is positive and σ_i is real, and both depend on θ and ϕ. The phase σ_i depends on the choice of the origin and on the sign conventions that have been adopted if polarised waves are involved. This point is emphasised because in the applications of scattering theory that follow individual polarisations are considered, and problems can be (and were) encountered if varying definitions are employed.

For spherical particles, by symmetry, it is the case that $S_3 = S_4 = 0$, and the diagonal elements, S_1 and S_2, depend only on the scattering angle, θ. In the applications that follow, the assumption of spherical particles is made.

3.2.4 Cross-sections and efficiency factors

The cross-section of some process, C_x, is defined as the ratio of the power removed by that process, W_x, to the incident beam intensity, I_i, and as such it has units of area:

$$C_x = \frac{W_x}{I_i} \tag{3.25}$$

For a beam incident on scattering particles there are two possible mechanisms for the removal of energy from the beam: 1) Scattering of photons out of the beam 2) Absorption of photons inside the particles. The cross sections for these processes are C_{sca} and C_{abs} respectively, and the total cross section for the extinction of the beam is given by:

$$C_{ext} = C_{abs} + C_{sca} \tag{3.26}$$

The corresponding efficiencies are defined as:

$$Q_{ext} = \frac{C_{ext}}{A}, \quad Q_{abs} = \frac{C_{abs}}{A}, \quad Q_{sca} = \frac{C_{sca}}{A} \tag{3.27}$$

where A is the cross-sectional area of the particle in the plane perpendicular to the direction of propagation of the incident beam. Thus for spherical particles $A = \pi a^2$, where a is the particle radius.

3.2.5 Single scatter albedo

The single scatter albedo is defined as:

$$\bar{\omega}_0 = \frac{C_{sca}}{C_{ext}} \tag{3.28}$$

It has a range of values of $0 \leq \bar{\omega}_0 \leq 1$.

3.2.6 The phase function

The phase function, $P(\theta, \phi)$, is a dimensionless function used to represent the angular dependence of scattered radiation. The phase function of unpolarised light is the ratio of scattered energy per unit solid angle in a given direction, (θ, ϕ), to the average energy per unit solid angle integrated over all solid angles. It is therefore normalised such that:

$$\frac{1}{4\pi} \int_0^{2\pi} \int_0^{\pi} P(\theta, \phi) \sin\theta d\phi d\theta = 1 \tag{3.29}$$

The intensity of the scattered wave in a particular direction can be calculated as $I(\theta, \phi) = I_i C_{sca} P(\theta, \phi)$, where I_i is the intensity of the incident plane wave.

For scattering by spherical particles the ϕ dependence is lost and the phase function can be expressed in terms of the diagonal elements of the amplitude scattering matrix as:

$$P(\theta) = \frac{2}{C_{sca}k^2l^2}(|S_1(\theta)|^2 + |S_2(\theta)|^2) \tag{3.30}$$

3.3 Mie theory

3.3.1 Method of derivation

Mie theory is the rigorous treatment of the scattering produced by a homogeneous sphere illuminated by plane wave electromagnetic radiation, and as such requires the application of Maxwell's equations. The full mathematical derivation will not be reproduced here, but can be found in texts such as *Bohren and Huffman* [1983]. The method by which the solutions are derived and the key results, however, will be summarised here.

The method of solution involves finding the solution to the vector wave equation (3.5) and applying the boundary conditions that the tangential components of **E** and **H** are continuous at the surface boundary of the sphere. Mathematically this is achieved as follows:

1. The wave equation is expressed in spherical coordinates, and the electric and magnetic fields inside and outside the sphere are expressed as a vector spherical expansion.

2. The boundary conditions at the surface of the sphere are then applied in order to obtain the scattered spherical wave Mie coefficients, a_n and b_n, which have no angular dependence.

3. The values of a_n and b_n can then be used to compute the extinction and scattering efficiencies, Q_{ext} and Q_{sca}.

4. The Mie angular functions, π_n and τ_n, which are defined in terms of Legendre polynomials and are a function of the scattering angle, θ, can then be used to obtain the scattering amplitude functions $S_1(\theta)$ and $S_2(\theta)$.

3.3.2 Mie amplitude functions

The scattering amplitude functions are given by:

$$S_1(\theta, x, \tilde{m}) = \sum_{n=1}^{\infty} \frac{2n+1}{n(n+1)}[a_n\pi_n(\cos\theta) + b_n\tau_n(\cos\theta)] \tag{3.31}$$

$$S_2(\theta, x, \tilde{m}) = \sum_{n=1}^{\infty} \frac{2n+1}{n(n+1)}[b_n\pi_n(\cos\theta) + a_n\tau_n(\cos\theta)] \tag{3.32}$$

The Mie angular functions, π_n and τ_n, are defined in terms of Legendre polynomials:

$$\pi_n(\cos\theta) = \frac{P_n^1(\cos\theta)}{\sin\theta} \tag{3.33}$$

$$\tau_n(\cos\theta) = \frac{d}{d\theta} P_n^1(\cos\theta) \tag{3.34}$$

The Mie coefficients, a_n and b_n, are given by:

$$a_n = \frac{\psi_n(x)\psi_n'(\tilde{m}x) - \tilde{m}\psi_n'(x)\psi_n(\tilde{m}x)}{\zeta_n(x)\psi_n'(\tilde{m}x) - \tilde{m}\zeta_n'(x)\psi_n(\tilde{m}x)} \tag{3.35}$$

$$b_n = \frac{\tilde{m}\psi_n(x)\psi_n'(\tilde{m}x) - \psi_n'(x)\psi_n(\tilde{m}x)}{\tilde{m}\zeta_n(x)\psi_n'(\tilde{m}x) - \tilde{m}\zeta_n'(x)\psi_n(\tilde{m}x)} \tag{3.36}$$

where ψ and ζ are the Ricatti-Bessel functions, defined as:

$$\psi_n(x) = \sqrt{\frac{\pi x}{2}} J_{n+\frac{1}{2}}(x) \tag{3.37}$$

and $J_{n+\frac{1}{2}}$ is the half-integral-order spherical Bessel function. Furthermore:

$$\zeta_n(x) = \sqrt{\frac{\pi x}{2}} H_{n+\frac{1}{2}}(x)^{(2)} \tag{3.38}$$

where $H_{n+\frac{1}{2}}(x)^{(2)}$ is the half-integral-order Hankel function of the second kind.

3.3.3 Mie efficiency factors

The Mie efficiency factors are derived from the scattering amplitude functions. The extinction efficiency is given by:

$$Q_{ext} = \frac{2}{x^2} \sum_{n=1}^{\infty} (2n+1) Re(a_n + b_n) \tag{3.39}$$

The scattering efficiency is given by:

$$Q_{sca} = \frac{2}{x^2} \sum_{n=1}^{\infty} (2n+1)(|a_n|^2 + |b_n|^2) \tag{3.40}$$

3.3.4 Mie scattering code

In the applications that follow, the AOPP IDL Mie scattering routine (found at: `http://www.atm.ox.ac.uk/code/mie/`) was used to compute the Mie scattering amplitudes. The code truncates the infinite series depending on the level of precision required. The IDL code allows double precision accuracy to be achieved.

3.4 The concept of an effective refractive index for a slab of many scatterers

3.4.1 The fundamental extinction formula

Consider the scattering produced by a single particle illuminated by an incident plane wave. Suppose that a detector is positioned in the forward direction, $\theta = 0$. In this forward direction, for spherical particles, we have that $S_1(0) = S_2(0) = S(0)$ due to the complete rotational symmetry about the z-axis. The scattered wave amplitude, E_s (where specification of the polarisation has been dropped due to the symmetry of the problem), is therefore given by:

$$E_s = S(0)\frac{e^{ikl}}{-ikl} \tag{3.41}$$

where $S(0) = s(0)e^{i\sigma(0)}$. A detector positioned in the forward direction observes the superposition of the incident plane wave and the scattered spherical wave. Suppose the plane of the detector is at $z = constant$ a large distance from the particle, and (x, y, z) is a point in this plane. Thus for a particle positioned at the origin the distance to the point (x, y, z) is given by:

$$l = z + \frac{x^2 + y^2}{2z} \tag{3.42}$$

The total amplitude, E, at the detector is formed by the superposition of the incident plane wave and the scattered spherical wave:

$$E = E_s + E_0 = E_0\left(1 + \frac{S(0)}{-ikl}e^{ik(x^2+y^2)/2z}\right) \tag{3.43}$$

The large distance to the detector implies that the second term in brackets is small. Then taking the squared modulus of this expression we find:

$$|E_s + E_0|^2 = |E_o|^2\left(1 + \frac{2}{kz}Re\left\{\frac{S(0)}{-i}e^{ik(x^2+y^2)/2z}\right\}\right) \tag{3.44}$$

The total intensity on the detector is the integral of this expression over the detector area in the (x, y) plane. The second term in this expression can be interpreted physically as the extinction of the beam manifest in the interference of the scattered and incident waves. As such the extinction coefficient is given by:

$$C_{ext} = \int_0^\infty\int_0^\infty \frac{2}{kz}Re\left\{\frac{S(0)}{-i}e^{ik(x^2+y^2)/2z}\right\}dxdy = \frac{4\pi}{k^2}Re\left\{S(0)\right\} \tag{3.45}$$

This is the fundamental extinction formula.

3.4.2 A slab of many scatterers

Perhaps the simplest derivation of an effective refractive index is that of H.C. van de Hulst for a slab of randomly positioned identical scatterers, which uses a simple extension of the derivation of the fundamental extinction formula.

Figure 3.2: Scattering in a slab containing many randomly located identical scatterers.

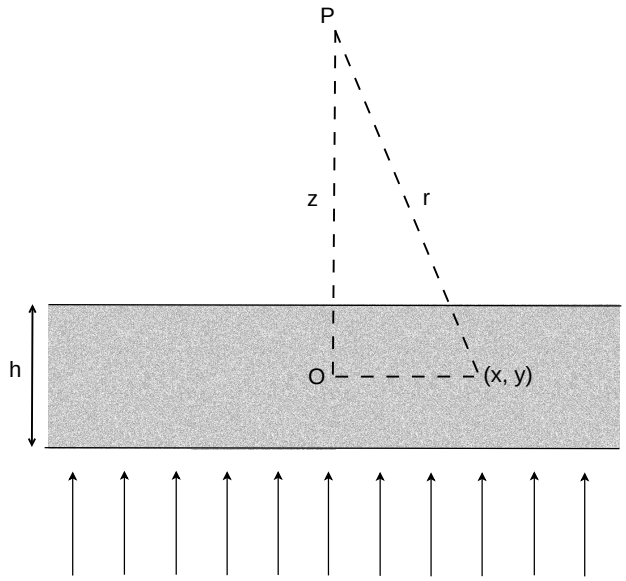

Considering the arrangement shown in Figure 3.2, it is argued that although the field at P is influenced by scattering from all the particles in the slab, the forward travelling wave is only influenced coherently by particles in a confined central region of the slab [*van der Hulst*, 1957]. It is further argued that if z is sufficiently large then only small angles will be involved, and the total amplitude at P, involving a summation over particles in the central region, can be expressed as:

$$E = E_0 \left(1 + S(0) \sum \frac{1}{-ikl} e^{ik(x^2+y^2)/2z}\right) \tag{3.46}$$

If we assume N, the number density of particles per unit volume, is sufficiently large, then the summation can be replaced by an integral of the form $\int N dx dy dz$, and direct integration yields:

$$E = E_0 \left(1 - \frac{2\pi}{k^2} NhS(0)\right) \tag{3.47}$$

If the slab were to be replaced by a homogeneous medium of refractive index, $\tilde{m}_{\text{eff}}$, with associated wavenumber, $\tilde{k}_{\text{eff}} = 2\pi\tilde{m}_{\text{eff}}/\lambda$, then the amplitude transmission coefficient of the slab is given by:

$$t_{\text{slab}} = \frac{E}{E_0} = e^{i(\tilde{k}_{\text{eff}} - \tilde{k})h} \tag{3.48}$$

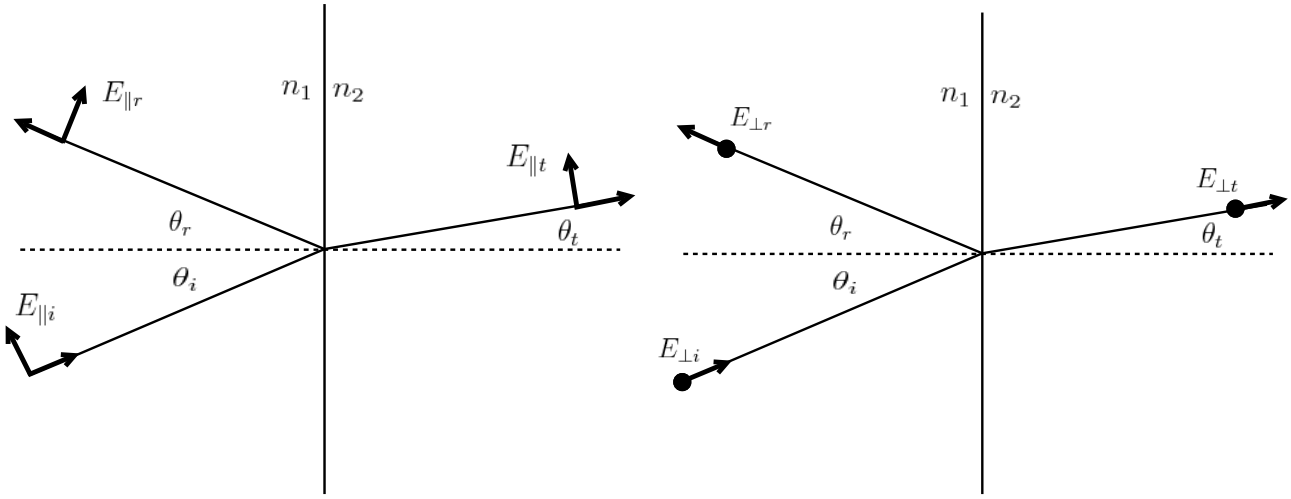

(a) Parallel polarisation **(b)** Perpendicular polarisation

Figure 3.3: Reflection and transmission at a plane boundary.

where $\tilde{k} = 2\pi\tilde{m}/\lambda$ is the wavenumber in the medium surrounding the particles, and this medium has refractive index $\tilde{m}$. Assuming that $\tilde{m}_{\text{eff}}$ is close to $\tilde{m}$, so that equation (3.48) may be expressed as the first two terms of its Taylor expansion, and then equating with equation (3.47) we obtain:

$$1 + i(\tilde{k}_{\text{eff}} - \tilde{k})h = 1 - \frac{2\pi}{\tilde{k}^2} hNS(0) \tag{3.49}$$

Consequently the effective refractive index of the slab of scatterers has the form:

$$\frac{\tilde{m}_{\text{eff}}}{\tilde{m}} = 1 + i\frac{2\pi}{\tilde{k}^3} NS(0) \tag{3.50}$$

A similar derivation to this is found in *Bohren and Huffman* [1983], but there it is argued that the result is only valid for particles with a small size parameter, x. Nevertheless the assumptions and failings of this simple approach will be discussed further in §4.1, and in §4.2 a more complete treatment will be introduced.

3.5 The Fresnel equations

The Fresnel equations express the reflectivity and transmission of light at the plane boundary between two half space containing different media. They are derived by first setting up the incident electromagnetic wave, applying the boundary conditions that the tangential components of **E** and **H** are continuous, and then solving for the resultant transmitted and reflected waves. This is done for both polarisations, i.e. for the case where the incident electric field is perpendicular to the incident plane[1], and for the case where it is parallel to the incident plane. The key results are summarised below[2]

[1]The incident plane contains the incident, reflected and transmitted waves and is perpendicular to the plane boundary between the two media.

[2]For a clear and complete derivation see *Hapke* [1993].

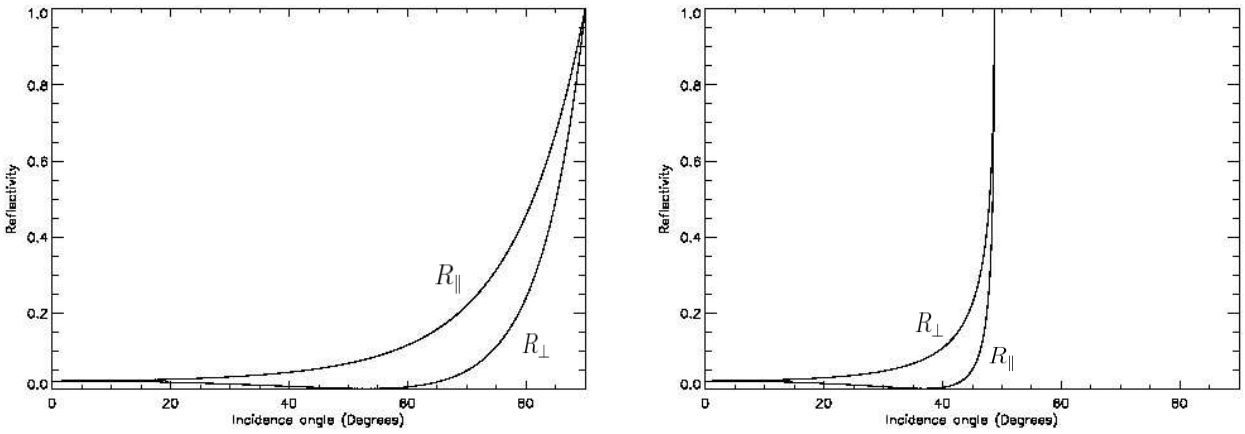

(a) **(b)**

Snell's Law relates the refractive indices of the two media, the incident angle, θ_i, and the transmitted angle, θ_t:

$$\tilde{n}_1 \sin(\theta_i) = \tilde{n}_2 \sin(\theta_t) \tag{3.51}$$

where n_1 and n_2 are the refractive indices of the initial and secondary medium respectively. The reflection is specular, i.e. $\theta_i = \theta_r$ where θ_r is the angle of reflection. The results for the complex amplitude reflection coefficients for the two polarisations are:

$$r_\perp = \frac{E_r}{E_i} = \frac{\cos(\theta_i) - \tilde{m}\cos(\theta_t)}{\cos(\theta_i) + \tilde{m}\cos(\theta_t)} \tag{3.52}$$

$$r_\parallel = \frac{E_r}{E_i} = \frac{\tilde{m}\cos(\theta_i) - \cos(\theta_t)}{\tilde{m}\cos(\theta_i) + \cos(\theta_t)} \tag{3.53}$$

where $\tilde{m} = \tilde{n}_2/\tilde{n}_1$, and E_i and E_r are the amplitudes of the incident and reflected waves respectively. These are related to the irradiance reflection coefficients, the ratio of reflected irradiance to the incident irradiance, via:

$$R_\perp = |r_\perp|^2 \tag{3.54}$$

$$R_\parallel = |r_\parallel|^2 \tag{3.55}$$

Chapter 4

A new refractometer method

4.1 Introduction

The aim of the device is to deduce optical properties, principally the refractive index, of an aerosol from angular measurements of the power reflectivity about an interface between an incident medium and a turbid medium containing the aerosol particles. In order to solve this inverse problem, we first must have a forward model that relates the measured angular reflectivity to the state vector of the system — namely the optical properties of the scatterers and the medium surrounding the particles, and the system geometry. Such a forward model must be derived from a theory that accurately describes the propagation of light in a system containing a random arrangement of scatterers.

Much work has been done developing models to describe the propagation of light in random media. In fact the paper, "On the transmission of light through an atmosphere containing small particles in suspension, and on the origin of the blue of the sky" by *Rayleigh* [1899], can be considered as one of the early examples. A considerable percentage of the work since then has concentrated on the construction of Effective Medium Theories (EMTs). Such theories assume that the propagation of the average electromagnetic field can be described in terms of effective optical coefficients (i.e. ϵ, μ and $n = \sqrt{\mu\epsilon/\mu_0\epsilon_0}$), which are assumed to be continuous functions of space inside the inhomogeneous medium. The aim of EMTs is to establish a relationship between the effective optical coefficients, the optical properties of the scatterers and the geometric properties of the system. These effective properties can then be used, within the framework of continuum electrodynamics, to determine results such as the reflectance and transmittance of the system. The derivation of the effective refractive index of a slab of many scatterers by *van der Hulst* [1957] (see §3.4.2) is an important example of such a theory, but a plethora of similar theories exists, notably those by *Garnett* [1904] and *Bruggeman* [1935]. However, theoretical and experimental investigations have shown that although valid for particles with small x, for particles with $x \geq 1$ an incorrect reflectivity and transmittance is obtained from inserting $\tilde{m}_{\text{eff}}$, derived from EMTs, into the Fresnel equations [*Bohren and Huffman*, 1983; *Barrera and García-Valenzuela-Valenzuela*, 2003; *Meeten and North*, 1995; *Bohnen*, 1986; *Mohammadi*, 1995].

A more complete treatment of the problem requires the application of wave theory to represent the multiple scattering in a random system, without necessarily employing the concept of an effective medium. There has been considerable work in this area, and the mathematical

techniques employed mostly invoke the T-matrix formalism and use N-particle Green's functions within the integral formalism of Maxwell's equations [*Tsang and Kong*, 1980, 1982; *Kuga et al.*, 1996; *Loiko et al.*, 2000]. These equations can be approximated to varying levels of accuracy depending on the level of statistical information available for the system. For example knowledge of the number density of scatterers, the two particle correlation function and the three particle correlation function, would correspond to increasing levels of accuracy. For the higher level models the computational time required makes them impractical for routine experimental measurements [*Barrera et al.*, 2005], and thus impractical here for the refractomoter device in question.

The theory that will be adopted for the forward model in this instance is the coherent scattering model (CSM) of *Barrera and García-Valenzuela-Valenzuela* [2003]; *Barrera et al.* [2005]. The model, which will be outlined in more detail in §4.2, uses standard wave scattering theory to calculate the coherent components of the fields radiated by a thin slab of randomly located scatterers in the dilute approximation (i.e. only knowledge of the number density of scatterers is required). Multiple scattering is then taken into account, in an average way, by integration over multiple thin slabs in order to construct a half space of the inhomogeneous medium.

4.2 CSM theory

A forward model is required that relates the measured angular reflectance about a suspension containing the aerosol particles to the optical properties of the particles, principally the real part of the refractive index of the particles. As discussed in the previous section, there has been a great deal of work in attempting to describe the propagation of light in materials containing random scatterers. A proper treatment requires the application of wave scattering theory.

The coherent scattering model (CSM) of *Barrera and García-Valenzuela-Valenzuela* [2003] offers a suitable approximation to the wave scattering equations for a dilute system of particles, but allows for particles with large size parameters. The complete mathematical derivation of the result is oulined in this paper and will not be reproduced here. However, the method, the important approximations, and the key results will be summarised here.

The mathematical derivation involves firstly computing the coherent reflected and transmitted waves for a thin slab of scatterers in the single scattering approximation. This means that the field exciting each particle is the incident field and the contribution from the scattering of all other particles is neglected. Multiple scattering in a half space of the scatterers is then taken into account by integration over consecutive slabs. These calculations assume that the width of consecutive slabs are small in comparison to the incident wavelength, and that the 2-particle correlation function (and higher order correlation functions) can be ignored. This means that the results are only valid for dilute systems of particles, which has important implications experimentally as will be discussed in more detail later.

The key result for the coherent amplitude reflection coefficient, r_{hs}, for a half space of randomly located, monodisperse particles, without any initial medium present (i.e. $n_1 = n_m$ and $\theta_i = \theta_m$, in figure 4.1), is given by:

$$r_{hs} = \frac{\beta}{i(k_z^{\text{eff}} + k_z^m) + \alpha} \tag{4.1}$$

Figure 4.1: Reflection from a suspension of scatterers. The refractive index of the initial medium is n_1. The particles have complex refractive index $\tilde{m}$. The initial medium and the medium in which the particles are suspended are assumed to be non-absorbing and so only the real parts are shown below: n_1 and n_m respectively.

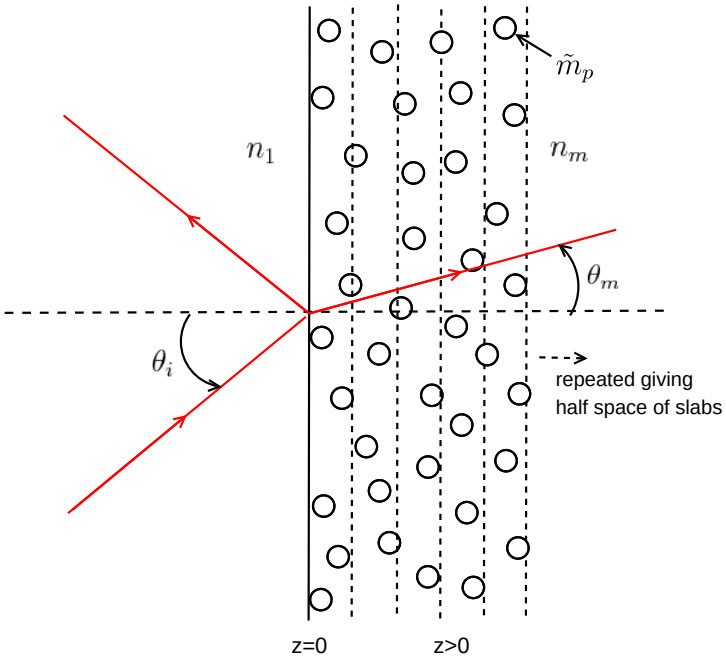

where α and β are related to the Mie scattering amplitude functions $S_j(\theta, x, \tilde{m})$ for a spherical particle (as defined in §3.2.3 and §3.3.2), and are given below. This is the result simply for a half space of scatterers, i.e. without an initial medium. Note that it is through $S_j(\theta, x, \tilde{m}_p)$ that the model's dependence on the optical properties of the particles, namely x and $\tilde{m}_p$, is realised. Note that the refractive index of the particles is complex, and so $\tilde{m}_p = n_p + \kappa_p$. Putting $j = 1$ or $j = 2$ gives the result for the perpendicular or parallel component with respect to the incident plane. We have that:

$$\alpha = \frac{-2\pi\rho}{k_m^2 \cos(\theta_m)} S(0, x, \tilde{m}_p) \tag{4.2}$$

$$\beta = \frac{-2\pi\rho}{k_m^2 \cos(\theta_m)} S_j(\pi - 2\theta_m, x, \tilde{m}_p) \tag{4.3}$$

and

$$k_z^m = k_m \cos(\theta_m) \tag{4.4}$$

$$k_m^{\text{eff}} = \sqrt{(k_z^m)^2 - 2i\alpha k_z^m + \beta^2 - \alpha^2} \tag{4.5}$$

where k_m is the wave number of light in the medium surrounding the particles, ρ is the number density of particles in the suspension, and θ_m is the direction of light in this medium. Note that when the initial medium is introduced into the model, such that there is a boundary between this and the turbid medium containing the particles, θ_m is then the angle of refraction (see Figure 4.1).

Experimentally we have control of the volume filling fraction, f, of the particles and this is related to the number density of particles, ρ, and the particle radius, a_0, via:

$$\rho = \frac{3f}{4\pi a_0^3} \tag{4.6}$$

Now let us consider what happens when we introduce the initial medium, placing the boundary at $z = 0$ and the turbid suspension at $z > 0$. The compound amplitude reflectance at the boundary is then given by:

$$r = \frac{r_{12}^{\text{Fresnel}} + r_{hs}(\theta_m)exp(2in_m k_0 \cos(\theta_m)a_0)}{1 + r_{12}^{\text{Fresnel}} r_{hs}(\theta_m)exp(2in_m k_0 \cos(\theta_m)a_0)} \tag{4.7}$$

where θ_m is obtained from Snell's Law:

$$\theta_m = \arcsin\left(\frac{n_1}{n_m}\sin(\theta_i)\right) \tag{4.8}$$

and where k_0 is the vacuum wavenumber and r_{12}^{Fresnel} is the Fresnel amplitude reflectivity that would arise at the boundary if the suspension contained no particles. It is worth noting at this point that the initial medium and the medium surrounding the particles are assumed to be non-absorbing and so only the real part of their refractive index need be considered: n_1 and n_m respectively (as in Equation 4.8). Additionally, note that r_{12}^{Fresnel} and r_{hs} must match (Equation 4.7), in the sense that they both refer to the same component of light with respect to the incident plane.

The phase factor $\exp(2in_m k_0 \cos(\theta_m)a_0)$ arises as a result of the condition that no particles protrude into the region $z < 0$, and hence the centre of all particles must lie in the region $z > a_0$ (see figure 4.1).

Taking the squared modulus of equation 4.7 yields the power reflectivity, $R = |r|^2$, the quantity measured by a detector. Equation 4.7 encapsulates the forward model, allowing the measured power reflectivity to be related back to the optical properties of the particles.

4.3 The relationship between sensitivity to refractive index and particle radius

The principle aim of the apparatus is to measure the refractive index of aerosol particles. It is therefore important to investigate how the sensitivity to refractive index depends on particle size, and for what particle size regime the apparatus and CSM can be used to make accurate measurements of refractive index.

Figure 4.2 shows reflectivity curves predicted by CSM. In all of the plots the particle volume filling fraction is fixed at $f = 4\,\%$ — chosen as a typical experimental value. The other physical parameters, excluding particle size and refractive index, are fixed at values representative of a typical experimental scan — for example, $n_m = 1.3316$ (the refractive index of the medium surrounding the particles is taken to be that of distilled water), $n_1 = 1.5150$ (the refractive index of the optic made from BK7 glass). Each plot shows CSM reflectivity curves for a different fixed value of the particle radius, a. Reflectivity curves for a range of refractive indices are

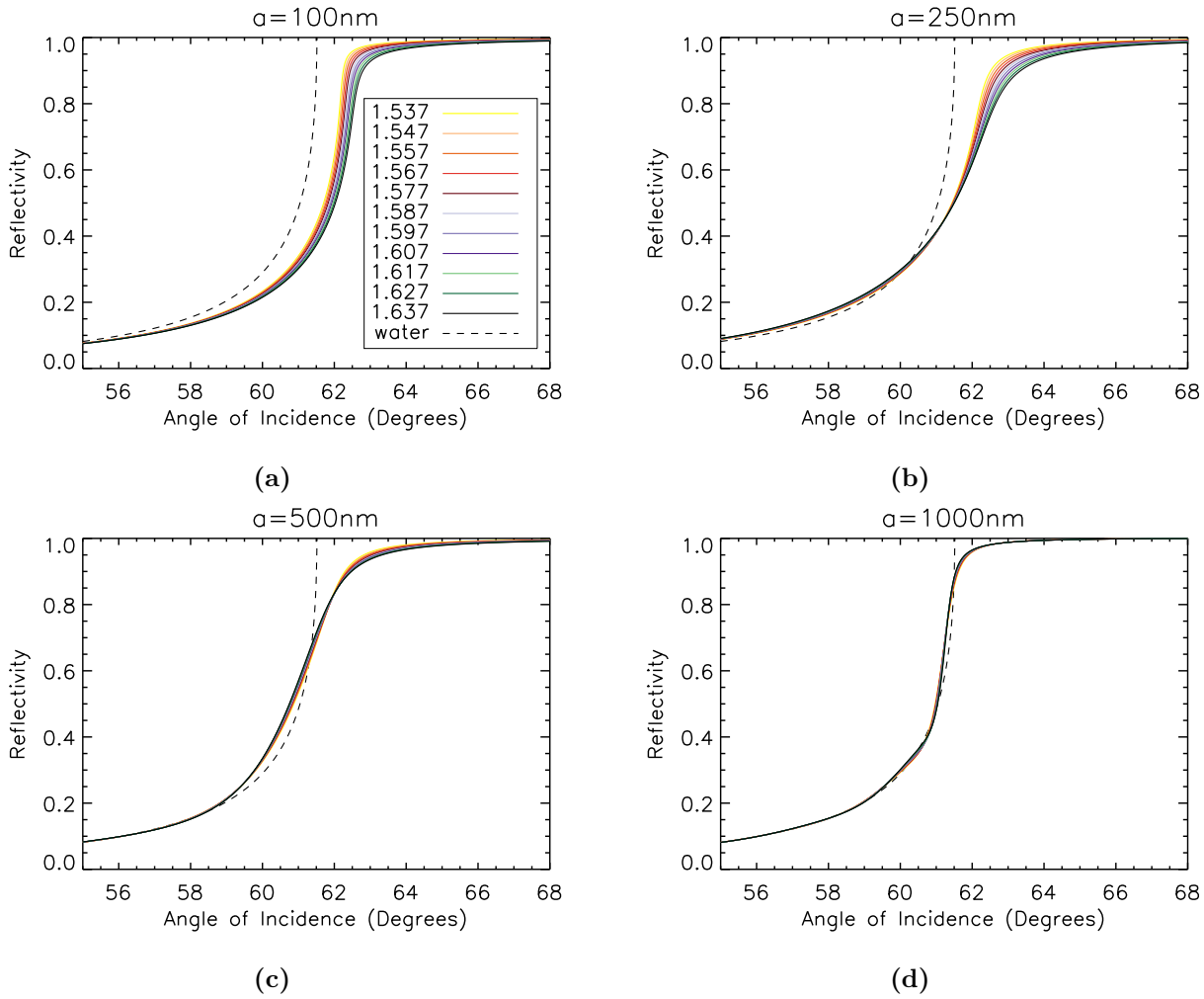

Figure 4.2: Reflectivity curves predicted by CSM for a monodisperse sample. Each plot shows CSM reflectivity curves for a different fixed value of the particle radius, a. Reflectivity curves for a range of values of the real part of the particle refractive index, n_{p}, are plotted with different colours as given in the key in Figure 4.2a. The other parameters are fixed at typical experimental values. The curves demonstrate that the sensitivity to particle refractive index is greatest for $a < 500\,\mathrm{nm}$.

plotted with different colours as given in the key in Figure 5.1a. The curves are centred on a particle refractive index of $\tilde{m}_p = 1.587 + 0.000i$[1], with a difference in the real part of the particle refractive index of 0.01 between successive curves.

The spread of the reflectivity curves in each graph gives a qualitative measure of the sensitivity to refractive index at the given value of the particle radius. It can be seen, with reference to Figures 4.2c and 4.2d, that the spread in reflectivity curves predicted by CSM is small for $a \geq 500\,\text{nm}$ indicating poor sensitivity to particle refractive index in this particle size regime. Furthermore, it can be seen that as the particle radius increases, the CSM reflectivity curves tend to approach the reflectivity curve expected from distilled water (i.e. with no particles present). This is a physically intuitive result, given that the mechanism of interaction of the particles with the incident light is Mie scattering and the Mie scattering cross section falls off rapidly when the particle radius is no longer comparable to the incident wavelength. Figures 4.2a and 4.2b demonstrate that the sensitivity to refractive index is greatest in the regime $a < 500\,\text{nm}$. In fact it is found that there is a very rapid reduction in sensitivity as the radius is increased above 450 nm.

This analysis is important because it demonstrates that the apparatus, in its current set up with a 635 nm laser diode, can be used to measure the refractive index of fine aerosol particles with a radius of less than 500 nm. However, note that the size parameter, $x = 2\pi a/\lambda$, is the determining parameter for the form of the curves in the figures, and therefore the sensitivity to refractive index would shift to larger particle radii if the wavelength of the laser diode were reduced.

4.4 The apparatus and experimental set up

Figure 4.3: Schematic of the basic experimental set up.

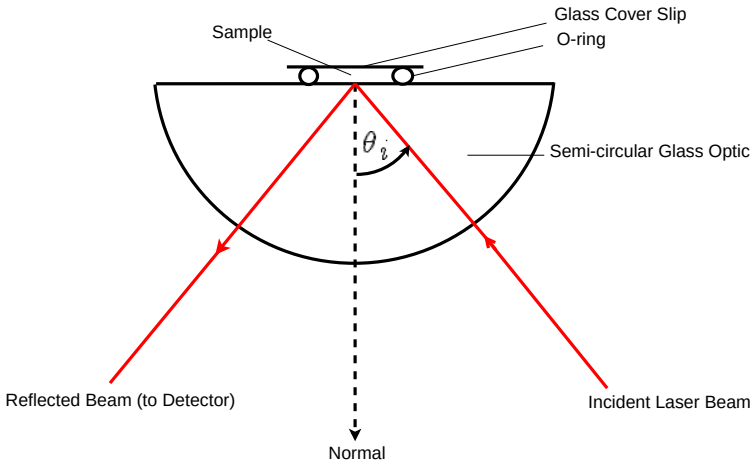

Figure 4.3 shows a schematic of the basic experimental set up. The suspension containing the aerosol particles is positioned on top of a semi-circular BK7 glass optic. The suspension is confined inside a rubber O-ring, with a glass cover slip placed on top to prevent losses due to evaporation.

[1]This is the refractive index of polystyrene at 635 nm - see §4.5.4 for the relevance of this particular value.

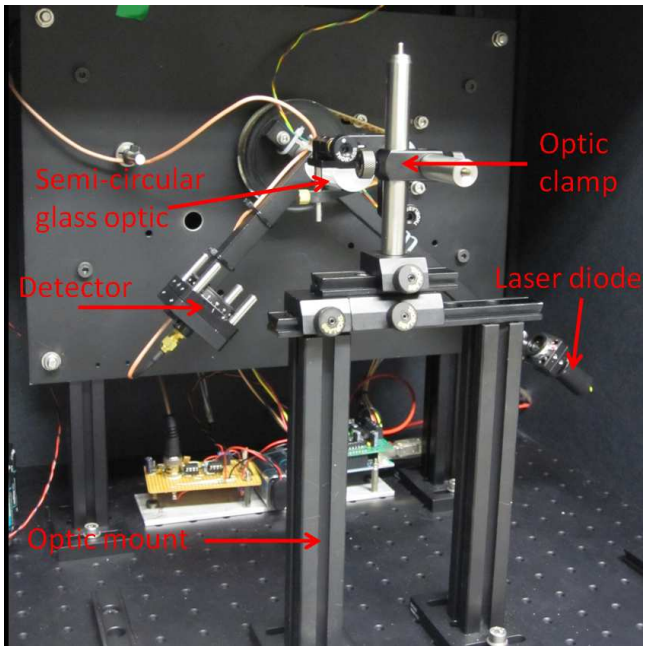

(a) Apparatus with optic mounted in position.

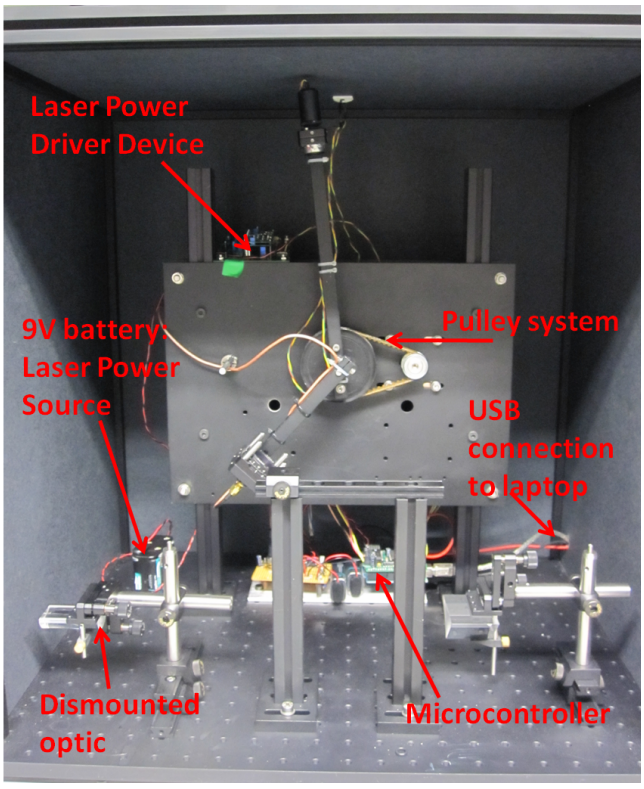

(b) Apparatus with optic dismounted.

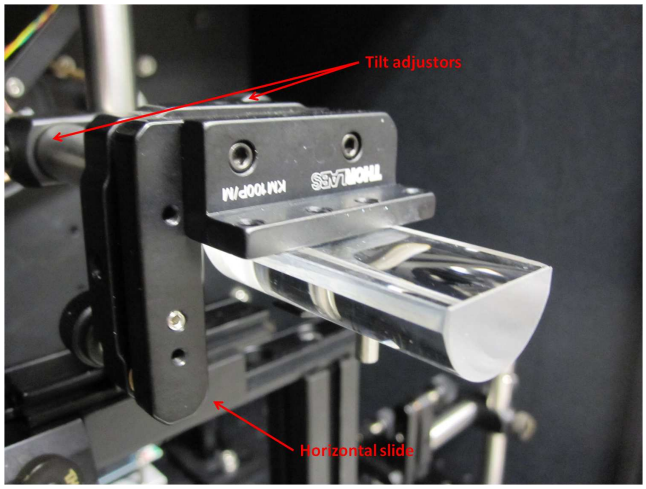

(c) The semi-circular glass optic.

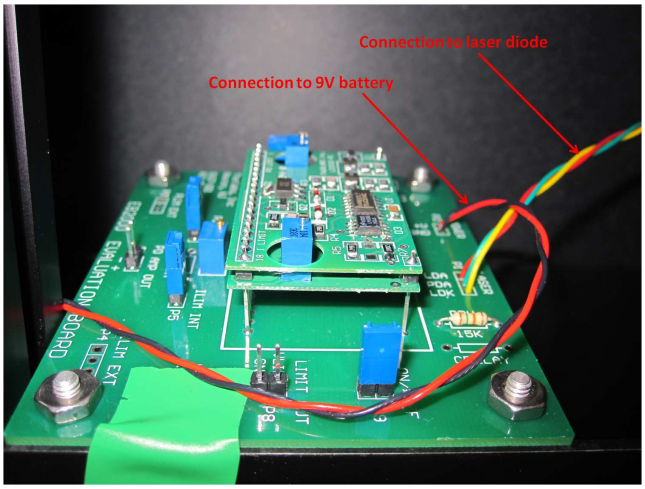

(d) Laser power driver kit (Thorlabs EK2000).

Figure 4.4: Photos of the apparatus.

A laser diode of wavelength 635 nm and a silicon photodiode detector are individually mounted on arms centred on the same point and able to rotate a full 360° about this point (Figures 4.4a and 4.4b). The angular positions of the arms are controlled by a stepper motor and a simple pulley system (Figure 4.4b). The stepper motors are controlled by a microcontroller which is connected via USB to a laptop (Figure 4.4b).

The laser diode is powered by a 9 V battery connected via a laser driver kit. The driver kit (see Fig 4.4d) uses a feedback loop that monitors the photodiode current (which is proportional to the laser output power) to regulate the laser output power. Uncertainty in the incident laser power will be considered in §4.4.1.

The detector has a polariser mounted in front, and this was set so that only perpendicularly polarised light (with respect to the optic flat surface) reached the detector. Thus all reflectivity data obtained in this paper are for $R_{\perp}$.

4.4.1 Laser power stability

Figure 4.5: Laser power variation with time.

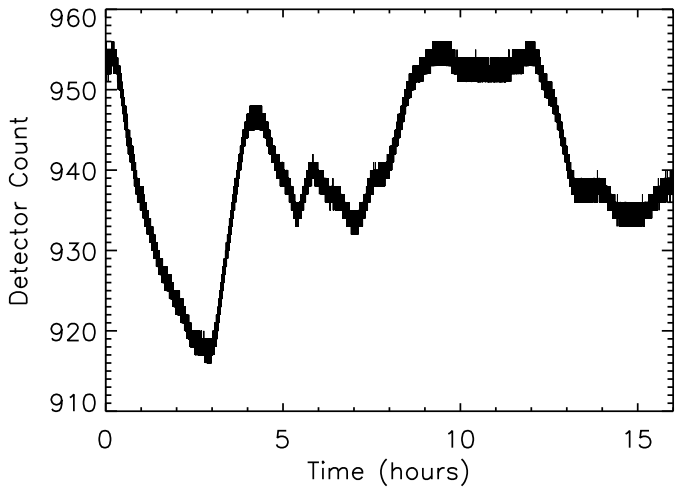

To test the laser power stability, the laser power was measured using the detector over a 16 hour period with a 0.2 s interval between detector readings. Figure 4.5 shows the result of this test: the detector count (proportional to irradiance incident on the detector) is plotted against time. The uncertainty in the photodiode detector response to a given irradiance is expected to be minimal in comparison with the laser power variation, and so it is assumed that the signal variation seen in Figure 4.5 is due to variation in the laser power. Figure 4.5 demonstrates a maximum variation in the laser power of approximately 4 % over the 16 hour period. This variation in laser power is significant, but it can be seen from Figure 4.5 that it corresponds to a systematic drift on a timescale of hours. There is a smaller scale noise superimposed onto this drift.

The detector count is proportional to the irradiance incident on the detector, so power reflectivity is calculated according to:

$$R = \frac{\text{Reflected Beam Detector Count} - \text{Background}}{\text{Incident Beam Detector Count} - \text{Background}} \tag{4.9}$$

As a result of the laser output variability there will be uncertainty associated with the value of the 'Incident Beam Detector Count' (equation 4.9) used to normalise the detector response to the reflected irradiance for each data point in the scan (a scan consists of a set of reflectivity measurements taken over a range of incidence angles, θ_i).

One possibility is to measure the reflected beam just before a scan commences for an incident angle such that there is total internal reflection, and then use this value as the value for the 'Incident Beam Detector Count'. It turns out, however, that instead of making a direct measurement, it is possible to have it as a retrieved parameter (without there being a significant increase in propagated uncertainties associated with other elements of the retrieved state vector). In either case, there is the assumption that the laser power remains constant for the duration of the scan over various incident angles, and it is therefore important to investigate the error introduced as a result of this assumption.

To investigate the uncertainty in our estimate of reflectivity calculated assuming that the laser power remains constant for the duration of a scan, the 16 hour laser power data were utilised. The scan duration and the time interval between scan measurements were needed. Firstly an initial location was randomly selected from the data. Then the deficits were calculated between the data detector count value and the initial value at subsequent succeeding regular time intervals, corresponding to the times of scan measurements. This process was repeated 5,000 times for various total scan times. The standard deviation in the deficits, σ_{LP}, gives the uncertainty in assuming a constant laser power. Table 1 summarises the results.

Scan Time (mins)	σ_{LP} in detector counts
10	1.13 (0.12 %)
20	2.09 (0.22 %)
40	3.77 (0.40 %)
60	5.38 (0.57 %)
90	6.74 (0.71 %)
120	7.21 (0.77 %)

Table 4.1: Shows the uncertainty in laser power, σ_{LP}, for various scan times given the assumption that laser power remains constant throughout the scan.

Table 1 shows that σ_{LP} increases steadily with scan time. A typical scan has a duration of 90 mins and so there is an uncertainty of $\sigma_{LP} = 0.71\,\%$ in assuming that the laser power remains constant throughout the scan.

4.4.2 Angular arm positions

The angular arm positions of the laser and detector are controlled by a stepper motor. Moving either arm 1256 steps will take it through a full 360° (so 1 step $\simeq 0.3°$ is the smallest angular resolution of the apparatus). To test the hypotheisis that the step locations are separated by equal angular increments, a digital level, accurate to 0.1°, was used to measure the angular

position of step locations at regular intervals of 10 steps. The angular level was zeroed on the base platform of the apparatus.

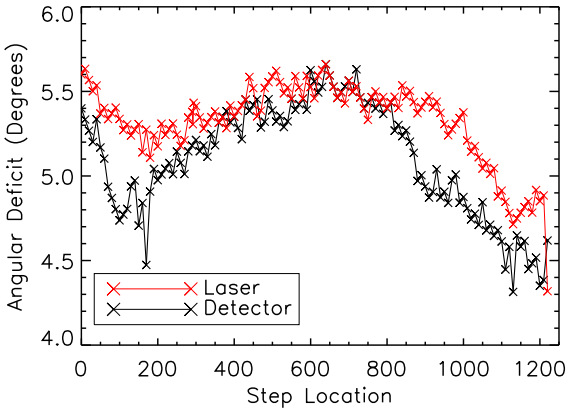

Figure 4.6: This graph illustrates the systematic variation in $\Delta\theta$ between step locations.

Figure 4.6 shows Angular Deficit, as defined below, plotted against Step Location.

$$\Delta\theta = \theta_{\text{measured}} - \theta_{\text{steps}} \tag{4.10}$$

where θ_{measured} is the angle measured by the digital level and θ_{steps} is the angle calculated using the step location and assuming a constant angle between step locations. For the constant angular interval hypothesis to be valid these plots should show a horizontal line[2], but it can be seen that this is not the case, indicating variation in the angle between step locations for both the laser and detector arms.

Figure 4.6 demonstrates the necessity to have an independent angular measure of each step location. The angular positions of all step locations for the detector and laser arms were measured, creating a look up table for use during data analysis.

4.5 Validating the experimental set up and CSM theory

4.5.1 Introduction to the general method

The aim is to measure the laser beam reflectance from the glass-sample boundary at the back surface of the semi-circular optic for a range of incidence angles. Inverse methods can then be used with the appropriate forward model to retrieve the required state vector elements. For example, Fresnel theory can then be used to retrieve the refractive index of a homogeneous sample, or CSM theory can be used for an aerosol suspension to retrieve aerosol optical properties. The experimental set-up is shown in Figure 4.3.

Proper alignment of the optic is essential to prevent systematic errors entering the data. For a perfectly semi-circular glass optic, the incident laser beam can enter and leave the glass

[2]Note that this horzontal line need not be at 0.0, due to the fact that θ_{measured} and θ_{steps} are zeroed relative to different reference points.

optic at normal incidence to the semi-circular surface, reflecting off the centre of the back surface. However, the optic used was not perfectly semi-circular - the centre of curvature of the back surface lies slightly above the top flat surface. However, the exact dimensions of the optic are known, meaning it is possible to apply a systematic correction to the experimental data negating this possible source of systematic error. The full details of this correction are given in appendix (insert). The correction given in appendix (insert) requires that the centre of rotation of the laser and detector arms is aligned with the centre of curvature of the optic's curved surface.

It is important to have an automated scan procedure to take data over a range of incidence angles. The microcontroller controls the arms' positions and the detector readings taken. Routines written in C are uploaded to the microcontroller via the USB port, and allow control of the scan.

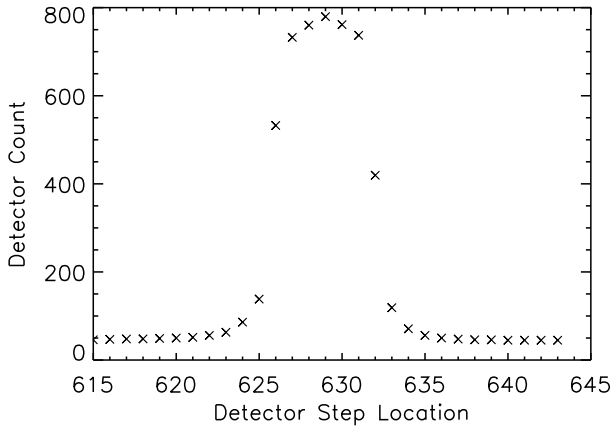

Figure 4.7: Laser beam profile. Plot generated by keeping the laser fixed and scanning the detector over the laser beam profile.

The laser beam has a degree of angular divergence giving a Gaussian-like profile (see Figure 4.7). Therefore for any particular incidence angle, θ_i, the detector must scan over a range of angles about $\theta_r = \theta_i$, thus capturing the profile and crucially the peak value. The range chosen was such that the entire reflected beam profile would be captured (i.e. until it reduces to the background level). The detector scan range for which this was the case was found to be ± 20 steps.

A typical scan is over a full range of incidence angles ($\theta_i = 0$ to $90°$), with a two step interval between laser arm positions (i.e. $\Delta\theta_i = 0.6°$). This step interval is a compromise between the gain of improved resolution and the associated increase in laser power uncertainty caused by the increased total scan time (see §4.4.1).

In summary for a typical scan, the successive laser step locations are separated by 2 steps, and for each laser position the detector scans ± 20 steps about $\theta_r = \theta_i$ and takes 10 readings at each of these detector positions.

4.5.2 Error propagation

For the general problem, the measurement vector, $\mathbf{y}$, is related to the state vector, $\mathbf{x}$, and the measurement error, ϵ, via:

$$\mathbf{y} = F(\mathbf{x}) + \epsilon \tag{4.11}$$

where $F(\mathbf{x})$ is the forward model (e.g. Fresnel Reflectance or CSM). After linearising this becomes:

$$\mathbf{y} = \mathbf{K}\mathbf{x} + \epsilon \tag{4.12}$$

where $\mathbf{K}$ is the Jacobian defined by $\mathbf{K}_{ij} = \delta F_i(\mathbf{x})/\delta x_j$, corresponding to the partial derivative of a forward model element with respect to a state vector element. The dimensions of $\mathbf{K}$ are $m \times n$, where m is the number of elements in the measurement vector and n is the number of retrieved parameters (i.e. the number of elements in the state vector).

The error covariance matrix associated with a vector is defined by $S_{ij} = \langle \epsilon_i \epsilon_j \rangle$, where ϵ_i is the uncertainty associated with the i-th element of the vector. The propagated uncertainty in the state vector elements is encapsulated by the state vector error covariance matrix, $\mathbf{S_x}$, which is related to the measurement error covariance matrix, $\mathbf{S}_\epsilon$, according to:

$$\mathbf{S}_\mathbf{x}^{-1} = \mathbf{K}^T \mathbf{S}_\epsilon^{-1} \mathbf{K} \tag{4.13}$$

There are two main sources of experimental error: uncertainty in the laser power over the duration of the scan (discussed in §4.4.1), and uncertainty in the angular positions of the detector and laser (§4.4.2). It is necessary to determine the uncertainty in the retrieved state vector elements for each type of experimental uncertainty via equation 4.13. These contributions to $\mathbf{S_x}$ can then be added linearly to give the total error covariance matrix for the state vector.

Firstly consider the construction of the error covariance matrix for the contribution from laser power uncertainty, $\mathbf{S}_{LP}$. The laser power uncertainty associated with each reflectivity detector count reading is a fixed percentage of this detector reading (see Table 4.1 in §4.4.1). The uncertainty arising from laser power variation associated with each reflectivity detector count measurement, R, is therefore given by $R\sigma_{LP}$ where σ_{LP} is a fixed fraction. The laser power error covariance matrix, $\mathbf{S}_{LP}$, will therefore be a diagonal matrix of variances where the i-th diagonal element is given by $\sigma_{LP}^2 R_i^2$, and R_i is the i-th element of the measurement vector $\mathbf{y}$ (i.e. the i-th measurement in the scan). The contribution to $\mathbf{S_x}$ from laser power uncertainty is therefore $(\mathbf{K}^T \mathbf{S}_{LP}^{-1} \mathbf{K})^{-1}$.

The uncertainty associated with each angular measurement is 0.1° (see §4.4.2), and so the angular error covariance matrix in angle space is given by $\mathbf{S}_A = 0.1\mathbf{I}$, where $\mathbf{I}$ is the identity matrix. The form of the covariance matrix in reflectivity measurement space is given by $\mathbf{B}\mathbf{S}_A\mathbf{B}^T$, where $B_{ij} = \delta F_i(\mathbf{x})/\delta\theta_j$ and θ_j is the incidence angle for the j-th element of the measurement vector $\mathbf{y}$. The contribution to $\mathbf{S_x}$ from angular uncertainty is therefor given by $(\mathbf{K}^T(\mathbf{B}\mathbf{S}_A\mathbf{B}^T)^{-1}\mathbf{K})^{-1}$.

Thus the total state vector error covariance matrix, a linear sum of the contributions from laser power uncertainty and angular uncertainty, is given by:

$$\mathbf{S_x} = (\mathbf{K}^T \mathbf{S}_{LP}^{-1} \mathbf{K})^{-1} + (\mathbf{K}^T(\mathbf{B}\mathbf{S}_A\mathbf{B}^T)^{-1}\mathbf{K})^{-1} \tag{4.14}$$

Table 4.2: Glass-Water error propagation results. It can be seen that the contribution from angular uncertainty dominates.

Error Term	Error Term Value	Propagated uncertainty in Re($\tilde{m}_{\text{water}}$)	Propagated uncertainty in Im($\tilde{m}_{\text{water}}$)
Laser Power	$\sigma_{\text{LP}} = 0.71\%$	0.000132	4.29×10^{-5}
Angular Arm Position	$\sigma_{\text{angle}} = 0.1°$	0.00102	0.000429

Propagated errors given in this report have been calculated using equation (4.14). Once $\mathbf{S_x}$ has been computed, the propagated variance, σ^2, associated with a particular element of the state vector can be extracted from the corresponding diagonal element of $\mathbf{S_x}$.

4.5.3 Glass and water measurements - Fresnel reflectance

In order to test the accuracy and overall performance of the equipment, independent of CSM theory, experiments were carried out using simple Fresnel reflectance at the back surface of the optic for two cases: for a glass-air interface (i.e. no sample present on the top surface of the optic); and for a glass-water interface.

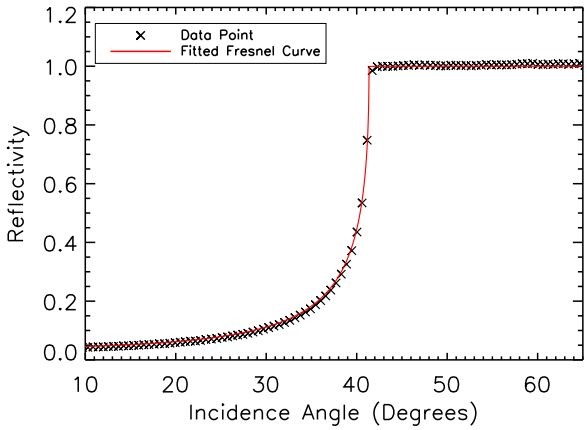

Figure 4.8: Glass-air scan, plot of $\perp$ irradiance reflectivity, $R_\perp$, against incidence angle, θ_i. The graph shows the experimental data and the fitted Fresnel curve in red. Fitted glass refractive index: $\tilde{m}_{\text{glass}} = 1.51332 + 9.2 \times 10^{-7} i$.

Figure 4.8 shows the data for the glass-air scan. Fresnel theory was used to fit the curve shown in red. A least squares fitting procedure was used, and both the real and imaginary parts of the glass refractive index were allowed to vary. The fitted value returned for the glass refractive index was $\tilde{m}_{\text{glass}} = 1.51332 + 9.2 \times 10^{-7} i$. The glass optic is made from BK7 glass, which has a known refractive index of $\tilde{m}_{\text{glass}}(\lambda = 635\text{nm}) = 1.51454 + 0.000i$ [*Sumitra Optical glass Inc.*, 2012]. So there is a discrepancy of $\Delta Re(\tilde{m}_{\text{glass}}) = 0.00122$ in the real part, and the imaginary parts are in agreement to 3 decimal places. The fitted result agrees with the value from literature to within propagated uncertainties.

Figure 4.9: Glass-water Scan #2, plot of $\perp$ irradiance reflectivity, $R_\perp$, against incidence angle, θ_i. The graph shows the experimental data and the fitted Fresnel curve in blue. Table shows data for fitted refractive indices for all 9 scans.

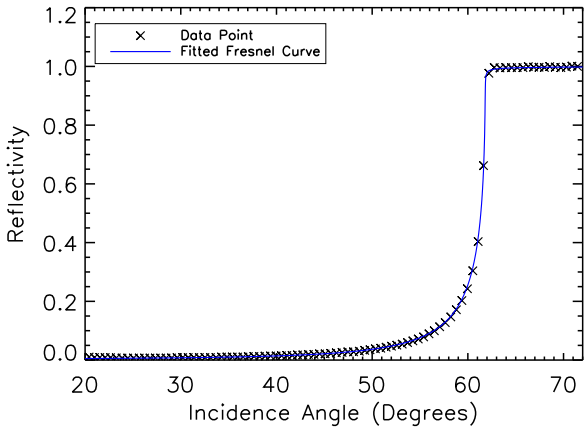

Table 4.3: Shows results of the Fresnel retrieval on the 9 repeat scans of the glass-water interface. The fitted values of $\mathrm{Re}(\tilde{m}_{\mathrm{water}})$ and $\mathrm{Im}(\tilde{m}_{\mathrm{water}})$ are shown, as well as the mean values for each and the standard deviation, σ, over the 9 scans.

Scan#	$\mathrm{Re}(\tilde{m}_{\mathrm{water}})$	$\mathrm{Im}(\tilde{m}_{\mathrm{water}})$
1	1.33198	0.00026
2	1.3321	0.00025
3	1.33239	0.00023
4	1.33243	0.00035
5	1.33242	0.00032
6	1.33246	0.00028
7	1.33251	0.00038
8	1.33242	0.00041
9	1.33237	0.00037
mean	1.33235	0.00032
σ	0.00017	0.00008

In addition tests were performed for a glass-water boundary, by pipetting several drops of distilled water onto the optic and covering with a glass slide to prevent evaporation losses (Figure 4.3). To determine the repeatability of the measurements, the glass-water scan was repeated 9 times in succession. Table 4.3 summarises the results. The mean fitted refractive index of water is $\tilde{m}_{\mathrm{water}} = 1.33235 + 0.00032i$, which compares well with the known value of $\tilde{m}_{\mathrm{water}} = 1.3316 + 0.0000i$ [*Hale and Querry*, 1973]. The discrepancies are $\Delta Re(\tilde{m}_{\mathrm{water}}) = 0.00075$ and $\Delta Im(\tilde{m}_{\mathrm{water}}) = 0.0003$. The discrepancies for all 9 scans are within experimental uncertainties shown in Table 4.2. It can also be seen from the standard deviation in the fitted values for the 9 scans that the repeatability of the measurements is very good.

The water and glass scans demonstrate that the apparatus can be used to retrieve the complex refractive index of a homogeneous substance to a high level of accuracy, and that the repeatability of these measurements is good.

4.5.4 Polystyrene spherical latex beads - CSM

Method

In order to verify the application of CSM for the retrieval of aerosol particle refractive index using the apparatus, tests were performed using test particles with known physical properties. The test particles used were spherical polystyrene latex beads produced by Sigma-Aldrich, UK. The samples provided were in a concentrated form with a quoted mass fraction value of 10 % w/w latex to water. The value of the mass fraction was independently measured for the particular sample. This was done by measuring a mass of the sample and then evaporating off the liquid to leave the polystyrene residue. The mass fraction was measured to be slightly higher than that quoted at 10.475 %. The supplier also states that the concentrated sample contains between 0.3 to 1.5 % of a soluble polymer[3], used to stabilise the particles against flocculation and agglomeration. The samples are essentially monodisperse: the 260 nm radius particles have a coefficient of variation in size of ≤ 3 %.

Figure 4.10: Characteristic reflectivity curve seen for a sample that has deteriorated with time. There is a typically a minima in such curves. Such a curve cannot be reproduced by CSM.

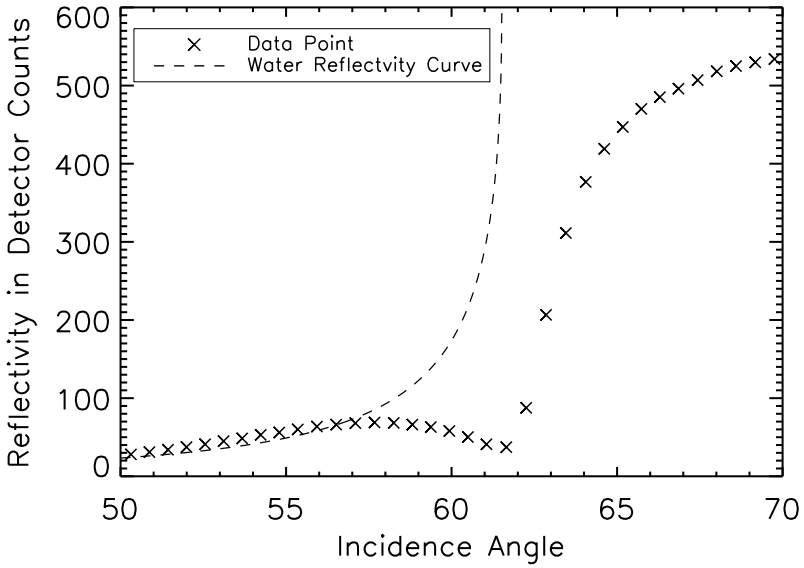

It was found that the sample preparation procedure was crucial in determining the quality of the data obtained. The 10 % w/w suspensions were held in an ultrasonic bath for 15 seconds before any samples were made up, as recommended by the manufacturer. This process is important to ensure that the polystyrene particles are evenly dispersed within the liquid. Diluted samples were made by pipetting several drops of the concentrated suspension into a vial, measuring the mass, then adding distilled water and re-measuring the mass (scales accurate to 0.0001 g were used). A micropipette and new clean pipette tip were used, in order to prevent contamination of the sample. The mass measurements allow the volume filling fraction, f, to be calculated for the latex particles in the diluted sample, according to the following formula:

[3]This is likely to change slightly the refractive index of the water.

$$f = \frac{c_l M_i/\rho_l}{c_l M_i/\rho_l + [(1-c_l)M_i + (M_t - M_i)]/\rho_l} \tag{4.15}$$

Where,

M_i = Initial mass of 10 %w/w sample

M_t = Total mass of distilled water + 10 %w/w sample

$\rho_l = 1.05$: Density of polystyrene

$\rho_w = 1.00$: Density of distilled water

c_l = measured w/w concentration of quoted 10 %w/w sample

The supplier of the polystyrene beads warns that the stability against agglomeration and flocculation may reduce if the beads are diluted. It is therefore important that the diluted samples were used immediately in the refractometer to obtain a reflectivity scan straight away. It was found that the diluted samples deteriorated with time once they had been made. This was apparent visibly for samples left for many hours as it could be seen that agglomerated particles were falling out of suspension, but also because the reflectivity curves produced from samples left for just a few hours were inconsistent with those expected from CSM. Figure 4.10 shows an example of the reflectivity data produced by a sample that has deteriorated with time. There is a characteristic minima in many of the reflectivity data taken for samples that had been left for a considerable period of time. Such a curve can not be produced by CSM, and is characteristic of a polystyrene latex bead sample that has deteriorated.

Therefore, in order to obtain reliable reflectivity data for the polystyrene latex beads, the scans were performed immediately after the diluted sample had been produced. CSM could then be used to retrieve the real part of the aerosol refractive index from the reflectivity data, as will be discussed in the following results and analysis section.

Results and analysis

A total of 5 scans were performed on the 260 nm radius polystyrene latex beads for volume filling fractions ranging from $f = 4.7\,\%$ to $f = 10.4\,\%$. CSM was then used to retrieve the real part of the particle refractive index, n_p, and the refractive index of the suspension liquid, n_m. The complex part of the refractive index, κ_p, was assumed to be negligible and fixed at zero — values from literature are < 0.001 [*Xiaoyan et al.*, 2003] and so are well outside the sensitivity of the apparatus (based on investigations of propagated error for an analysis where κ_p is a retrieved parameter). It was chosen to have n_m as a retrieved parameter rather than using the value for the refractive index of distilled water. The reason for this is the concentrated latex suspension supplied by the manufacturer contains a concentration of between 0.3 to 1.5 % of a soluble polymer (to minimise agglomeration and flocculation), which is likely to change slightly the refractive index of the liquid.

Table 4.4 shows the CSM retrieval results for the 5 scans performed for various volume filling fractions. The mean refractive index from the 5 scans is $\langle n_p \rangle = 1.5937$, which compares well with the known value from literature of $n_p(\lambda = 635\,\text{nm}) = 1.5870$ [*Kasarova et al.*, 2007] and to within the propogated uncertainty of 0.0106. The contributions to the propagated uncertainties are shown in Table 4.5.

Figure 4.11 shows three of the reflectivity scans for the polystyrene latex beads. In each graph the experimental data points are shown and the fitted CSM curve is plotted as well as

Table 4.4: CSM retrieval results for the 5 polystyrene latex bead scans at various volume filling fractions, f. The table shows the retrieved value of the refractive index of the suspension liquid, n_m, and the retrieved value of the particle refractive index, n_p.

Volume filling fraction, f	Retrieved value of n_m	Retrieved value of n_p
0.04747	1.3363	1.6045
0.06204	1.3337	1.5932
0.06699	1.3359	1.5933
0.08268	1.3379	1.5868
0.10364	1.3398	1.5906

Table 4.5: Error propagation results for the polystyrene latex bead retrieval.

Error Source	Propagated uncertainty in n_p
Laser power variation, $\sigma_{LP} = 0.71\,\%$	0.0076
Angular uncertainty, $\sigma_A = 0.1^\circ$	0.0141
Combined uncertainty	0.0160

the reflectivity curve expected of pure water. In addition the reflectivity curve is shown for a liquid with the retrieved value of n_m (i.e. the value shown in Table 4.4). It can be seen that as the volume filling fraction increases the shape of the reflectivity curve changes, and the deviation from the water reflectivity curve becomes more pronounced. The three graphs of Figure 4.11 demonstrate that CSM provides a good fit to the experimental reflectivity data.

The tests performed using the polystyrene latex beads demonstrate that the apparatus and the application of CSM can be used to retrieve the refractive index of spherical particles of a known radius to a good level of accuracy. The tests replicate those performed by *Barrera and García-Valenzuela-Valenzuela* [2003].

Figure 4.11: 3 Reflectivity scans of the polystyrene latex spheres. The fitted CSM curve is shown in each, as well as the reflectivity curve expected of pure water. In addition the reflectivity curve is shown for the retrieved value of n_m — labelled as 'fitted liquid' in the key.

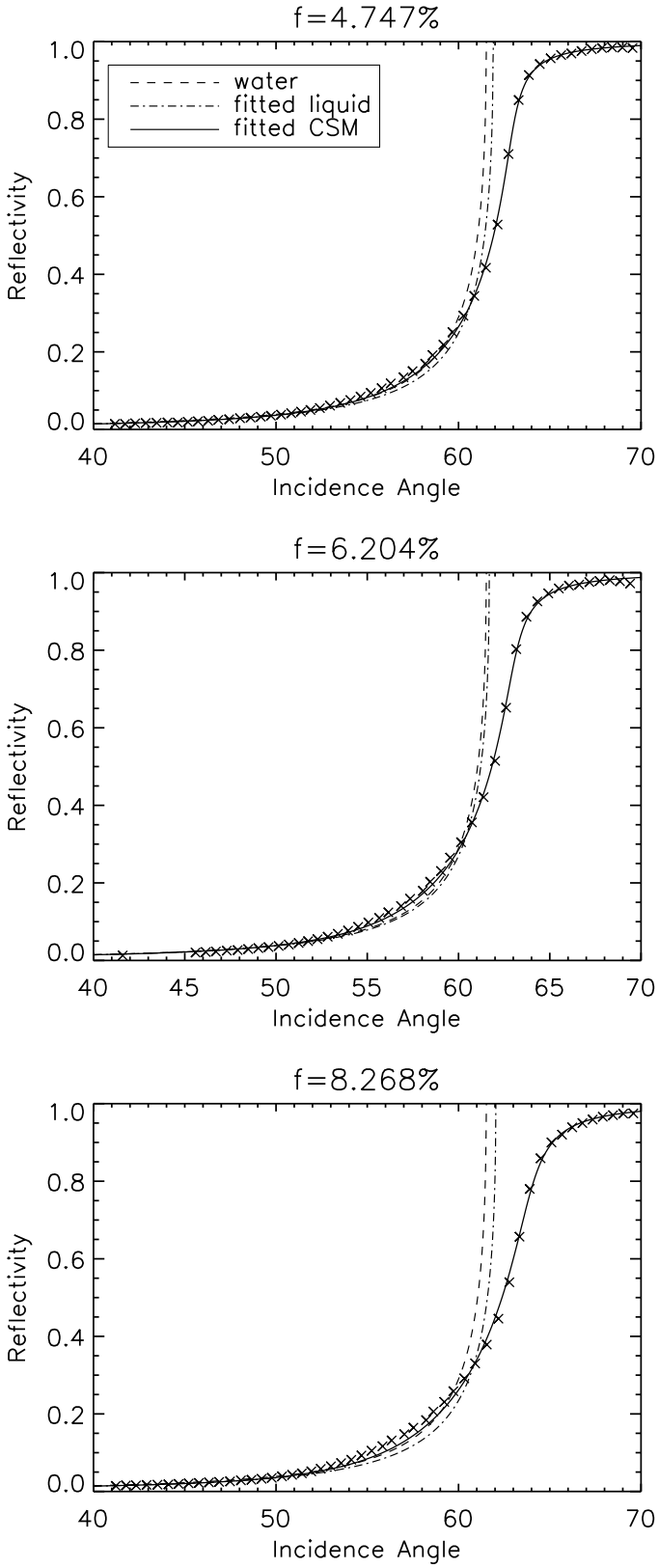

4.5.5 Application of CSM to 'ash-like' commercial sand

Method

A typical aerosol sample of interest to atmospheric physicists, for example a sample of volcanic ash, is not monodisperse with respect to particle size. It is also typically the case that the particle size distribution is unknown. As outlined in §4.3, there is a particle size 'window' for which the reflectivity curve, predicted by CSM, is sensitive to refractive index, and for which the reflectivity curve differs appreciably from that of pure water. Tests were performed using a commercial sand sample to determine whether the CSM retrieval assuming a monodisperse distribution could obtain physically sensible results for particle optical properties. Furthermore, the same sand sample was tested using the microscopic Becke line method (see Chapter 5) to provide an independent measure of the particle refractive index.

The analysis discussed in §4.3 demonstrates that there is sensitivity to refractive index for particles with a radius of less than 500 nm. It is therefore necessary, before reflectivity scans can be performed, to separate this fine material from the larger coarse material ($a > 500$ nm).

A sedimentation technique was adopted in order to separate off the fine material. A mass of approximately 200 grams of the commercial sand sample was first evenly dispersed in approximately 800 ml of distilled water. Ultrasonic agitation was used to ensure even dispersal of the sample in the distilled water. The mixture was then left to settle in an Imhoff cone (see Figure 4.12) for 24 hours - the higher Stokes settling velocity of larger particles results in these particles falling out of suspension more rapidly, and the Brownian motion of finer particles tends to dominate over settling helping these particles to remain in suspension.

Figure 4.12: Imhoff cone containing the commercial sand in distilled water after 24 hours of settling. It can be seen that a considerable mass of course material has accumulated at the bottom, leaving the finer material still in suspension.

The fine material still remaining in suspension after the 24 hour period was drawn off. This suspension was then gently heated in a beaker to encourage evaporation of the water. This was done until only the solid deposit of fine sand particles remained. The fine ash sand could then be used to make up suspensions of various concentrations, for testing with the refractometer.

Figure 4.13: 20x objective microscope images of the commercial sand sample before and after the sedimentation technique was used to remove the course material. The width of the images is approximately 300 μm.

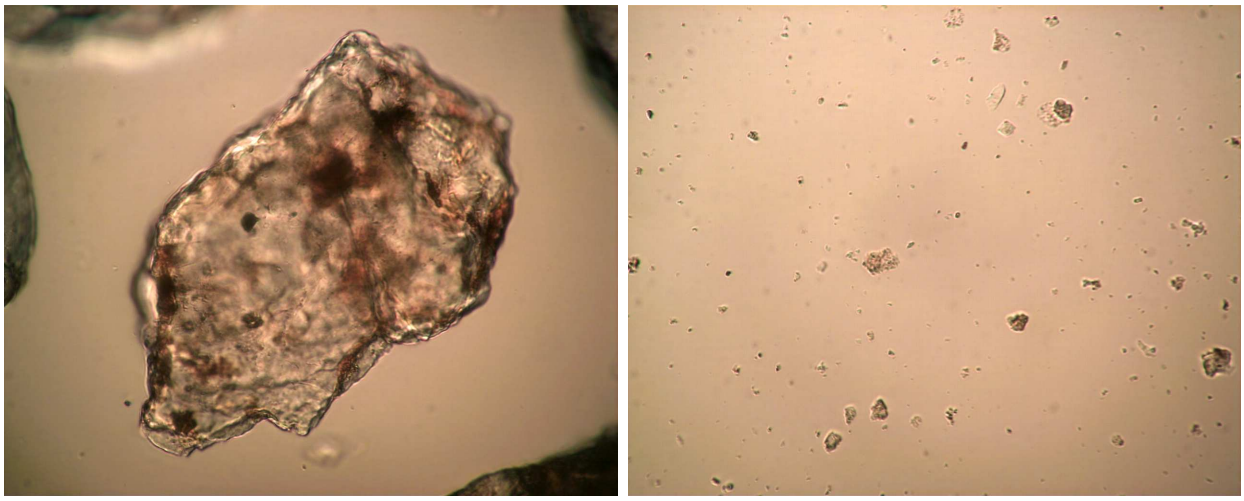

(a) Before: Image dominated by very large particles with width comparable to microscope field of view.

(b) After: Largest particles have been removed leaving fine material.

A distilled water suspension of the fine and of the bulk sand sample were also made up, in order to be viewed under an optical microscope.

It can be seen from the microscope images shown in Figure 4.13, taken of the sample before and after the sedimentation technique was used to remove the course material, that the process is effective in removing the large particles that constitute the vast majority of the mass of the initial sample. In fact from an initial mass of 200 grams of the bulk sand sample, only a mass of 0.23 grams of fine material was left in suspension after the 24 hour period. This has important practical implications for the application of the technique to volcanic ash samples.

With confirmation from the microscope images that the sedimentation process had been successful at separating off the fine material, it was now possible to perform refractometer scans on the fine separated sample. With no a priori information about the properties of the sand (size distribution, density etc.) it was not possible to produce a suspension of known volume filling fraction from simple sand and water mass measurements. A somewhat trial and error process was adopted in order to produce a suspension of the fine particles with a volume filling fraction, f, suitable for an accurate retrieval using CSM. The sample must be sufficiently dilute such that the dilute approximation of CSM remains valid, but sufficiently concentrated in order for there to be a significant deviation in the reflectivity signal from that of pure water. Initially a highly dilute suspension of the fine sand particles was made, and a reflectivity scan was performed by placing a few drops of the dilute sample onto the refractometer optic. It could then be seen by analysing the resultant reflectivity curve that there was very little deviation from the reflectivity curve expected of pure water. As a result the sample was concentrated by evaporating off some of the distilled water by gentle heating. These steps were repeated until the sample was concentrated enough to give a reflectivity signal that deviated sufficiently from that of pure water. Once this correct concentration was achieved, repeated reflectivity scans were performed on the sample.

Figure 4.14: Commercial sand typical reflectivity curve: Scan No. 5. The graph shows the fitted CSM curve as well as the reflectivity curve expected of pure water.

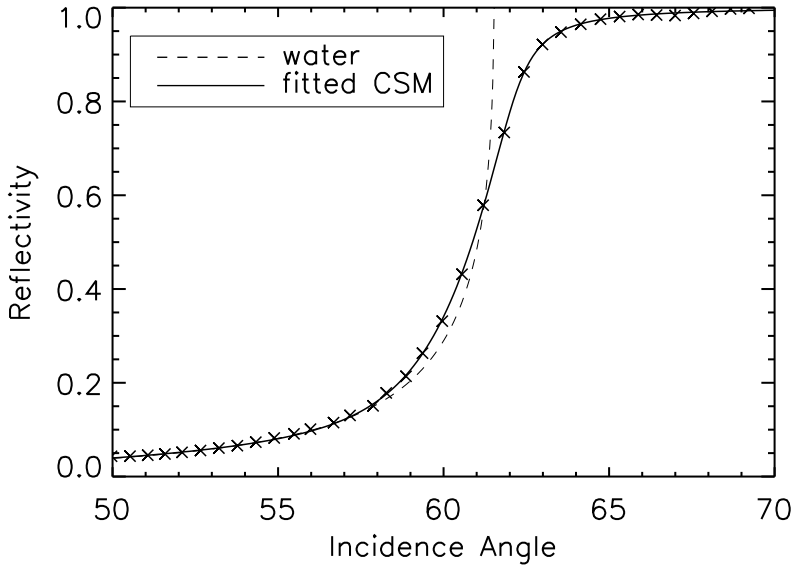

Results and analysis

Given that there is no a priori knowledge about the physical properties of the fine separated sand sample, it is necessary to use CSM to retrieve the particle radius, a, the particle refractive index, n_p, and the volume filling fraction, f, of particles in the suspension when analysing the reflectivity scan data.

Table 4.6: Table of retrieved parameters — a, f and n_p — using the CSM forward moded for the 6 reflectivity scans performed on the fine separated sand sample.

Scan No.	Particle Radius, a	Volume filling fraction, f	Particle Refractive index, n_p
1	379	0.0468	1.586
2	381	0.0417	1.550
3	435	0.0456	1.585
4	435	0.0470	1.589
5	366	0.0496	1.557
6	340	0.0461	1.568

Table 4.6 summarises the results of the CSM retrieval on the fine separated sand reflectivity data. Figure 4.14 shows the reflectivity curve for scan No. 5. The mean particle refractive index retrieved from the 6 scans is $\langle n_p(\lambda = 635\,\mathrm{nm})\rangle = 1.572$. Table 4.7 summarises the error propagation results for the retrieval. It can be seen that the propagated uncertainty is considerably larger than for the polystyrene latex bead retrieval, owing to the additional parameters retrieved in this case.

Microscopic Becke Line tests were also performed on the same fine separated sand sample. A full description of the Becke Line tests performed is outlined in Chapter 5. The technique

makes use of the lensing effect of particles submersed in a liquid, and by comparing the effect with different liquids of known refractive index it is possible to determine the mean particle refractive index for particles in a sample. As given in Table 5.1 the mean particle refractive index, as determined by the Becke Line technique, for the fine separated sand sample was found at two different wavelengths to be: $n_p(\lambda = 546.1\,\text{nm}) = 1.566 \pm 0.01$ and $n_p(\lambda = 650.0\,\text{nm}) = 1.560 \pm 0.01$. Linear interpolation, using these two Becke Line data points, to the refractometer laser diode wavelength of 635 nm gives a value of $n_p(\lambda = 635\,\text{nm}) = 1.561$. It can be seen that the Becke Line results compare well with the mean value from the 6 reflectivity scans of $\langle n_p \rangle = 1.572$, and to within the propagated uncertainty of 0.0267.

Table 4.7: Error propagation results for CSM sand retrieval.

Error Source	Propagated uncertainty in n_p
Laser power variation, $\sigma_{LP} = 0.71\,\%$	0.0136
Angular uncertainty, $\sigma_A = 0.1^\circ$	0.0230
Combined uncertainty	0.0267

It is worth noting, however, that the Becke Line and the refractometer techniques apply to different particle size regimes, so some caution is due when comparing the results. As outlined in §5.3.1, the Becke Line method is limited by the resolving power of the optical microscope, and so the mean particle refractive index derived from these measurements is valid for particles with $a \geq 500\,\text{nm}$. In contrast the analysis of §4.3 demonstrates that the CSM retrieval is sensitive to refractive index for particles with $a < 500\,\text{nm}$, consistent with the mean value retrieved from the 6 reflectivity scans of $\langle a \rangle = 389\,\text{nm}$. It is, however, not unreasonable to assume that the composition, and therefor refractive index, of the commercial grade sand is uniform with respect to particle size.

The results from the sand scans are by no means exhaustive, but they suggest that the monodisperse CSM forward model can be used to retrieve physically sensible particle optical properties. The value for the particle refractive index retrieved agrees with the value obtained from the Becke Line method to within experimental uncertainty. To my knowledge, CSM has not been applied in this way before.

It is possible to extend the theory of CSM to non-monodisperse size distributions [*Barrera et al.*, 2005]. This, however, would require accurate size distribution knowledge for the sub 500 nm radius particles. This is an area for future investigation.

Chapter 5

The Becke line method

5.1 Introduction

The Becke line method can be utilised to determine the real part of the refractive index of aerosol particles with diameters $\geq 1\,\mu$m (as determined by the resolution limit of the microscope).

The Becke line is an optical phenomenon associated with the interface between two substances with differing refractive indices observed on the stage of a microscope. The Becke line is observed when the sample is illuminated from below by slightly diverging or converging light. This is best achieved with a long focal length condensing lens and with the substage aperture diaphragm stopped down to render the incident light nearly parallel and to limit the total amount of illumination.

The Becke line method relies on the principle that for a fragment of aerosol surrounded by liquid, total internal reflection and refraction act together to produce a concentration of light close to the fragment–liquid interface on the side towards the medium of higher index. This concentration of light forms the Becke line.

The Becke line is not visible when the fragment is perfectly in focus. However when the objective lens is raised (or the stage is lowered), the Becke line will appear to move into the material with the higher refractive index. Conversely, if the objective is lowered (or the stage raised) then the Becke line will appear to move into the material of lower refractive index. If the refractive index of the liquid is perfectly matched with that of the aerosol fragment then no Becke line will be visible.

Thus a given aerosol sample can be systematically checked against liquids of known refractive indices, to determine whether the sample has a higher or lower refractive index than that of each liquid. Typically the sample refractive index is found to sit between two refractive index liquids, although a perfect match with the sample may also be observed. There is also typically a degree of inhomogeneity with respect to composition and therefore in refractive index in, for example, a typical volcanic ash or dust sample. A detailed description of the experimental method adopted is given below.

5.2 Experimental method

5.2.1 Wavelength dependence and coefficient of variation with temperature of the refractive index liquids

The refractive index matching liquids used in the tests on aerosol samples were manufactured by Cargille Laboratories. The liquids used were incremented by 0.01 in refractive index, and covered a range of refractive indices from $n = 1.50$ to $n = 1.80$.

The Becke line test was performed on each sample at 3 different wavelengths in the visible: 450 nm, 546.1 nm and 650 nm. This was acheived using filters placed in front of the digital camera sensor. Each filter used had a bandwidth of ± 10 nm about the peak transmittance values given above. The liquid refractive indices are standardised and quoted at a wavelength of 589.3 nm. The Cauchy equations for the liquids were supplied, so that the refractive index at a given wavelegth could be established.

The liquid refractive indices are also standardised and quoted for a temperature of 25 °C. The coefficient of variation with temperature of the liquids is known, so that the refractive index of the liquid at a given temperature could be calculated. In all the tests performed a thermometer was placed near to the microscope stage to monitor the temperature.

5.2.2 Sample preparation

A clean spatula or pipette tip was used to transfer a small quantity of the ash or dust sample into a clean vial. No more than approximately 2 to 3 ml of the refractive index liquid was then added to the vial using a micropipette with a clean tip. Care was taken to prevent contamination of the refractive index liquids: a clean pipette tip must be used and the time that the liquid's jar is left open must be minimised.

It is important that the aerosol particle number density in the mixture is not too high, so that when viewed under the microscope the fragments are not agglomerated and so that fragments completely surrounded by liquid can be seen. However, the particle number density should not be too low, as it is useful to check the Becke line displacement for multiple particles in the field of view — this allows the degree of inhomogeneity in the sample to be analysed.

The aerosol sample and liquid mixture was shaken vigorously to disperse the particles evenly in the liquid. A few drops of the mixture were then placed onto a clean glass slide and a glass slip placed on top. The sample slide could then be placed on the microscope stage for viewing.

5.2.3 Optimal microscope set up for viewing the Becke line

The Becke line is best observed when the sample is illuminated from below by slightly converging or diverging light. This is achieved by employing a long focal length condensing lens and by stopping down the substage aperture diaphragm. A 20x objective was used for all of the Becke line tests performed. A halogen light provided white light substage illumination. The sample was viewed via the digital camera on the computer monitor.

Firstly it was necessary to check that the condensing lens and aperture were aligned with the objective lens along the optical axis. Then, with the aerosol fragments in focus, the vertical

height of the condensing lens was adjusted to give a uniform illumination of the field of view. With the halogen light brightness set to its maximum value and with the chosen wavelength filter in place in front of the camera sensor, the substage aperture diaphragm was stopped down to nearly the smallest aperture — the criteria being to maximise the contrast and visibility of the Becke line at the edges of aerosol fragments.

5.2.4 Particle sizing

It is necessary to determine the range of particle sizes for which the refractive index measurements made are applicable. Images of a graticule were recorded in order to determine the range of particle sizes for which the Becke line was resolvable: The graticule images were compared with particle Becke line images. The graticule used had a smallest increment of 10 μm. Cropped images of the graticule were compared to identically cropped images of aerosol samples in refractive index liquids, in order to deduce the minimum particle size for which the Becke line is just resolvable. The results of this analysis are presented in section 5.3.1.

5.2.5 Becke line method for an aerosol sample

- Firstly a slide of the sample was prepared in the 1.5000 refractive index liquid. A different starting liquid was sometimes chosen if it was believed likely closer to that of the sample.
- With one of the three available filters in position, the Becke line displacement of fragments in the field of view were checked by raising or lowering the objective lens. Thus it was determined whether the sample refractive index was higher or lower than that of the liquid at that particular wavelength. The Becke line displacement for the same particles was checked at each of the three wavelengths — 450 nm, 546.1 nm and 650 nm — by putting in place the appropriate filter.
- Still images of the Becke line displacement as the objective lens was raised were recorded, so that they could be re-analysed and checked later. This becomes particularly useful when there was a significant degree of inhomogeneity in the sample and when the mean particle refractive index was close to that of the liquid.
- The contrast of the particle image is greater when there is a larger difference in refractive index with the liquid: with some experience, it becomes possible to estimate how much higher/lower the particle refractive index is.
- The refractive index of particles in a typical sample of volcanic ash has a degree of inhomogeneity. When the refractive index of the particles differs greatly from the liquid then the particle contrast is high and the Becke line displacement is in the same direction for the vast majority of particles. However when the refractive index of the liquid is close to the mean particle refractive index, then the particles appear faint and there may be a significant minority of particles for which the Becke line displacement opposes that of the majority of particles.
- The task of determining the mean particle refractive index is simpler when the sample is nearly homogeneous. In this case systematically checking the particles against the

Figure 5.1: In images (a), (b), (c) to (d) the objective lens is increasingly raised and the Becke line is seen to move into the particles - demonstrating that they have a higher refractive index than the liquid. In this case the fragments shown are Cape Verde Dust in 1.50 refractive index liquid, and the 546.1 nm filter is in place.

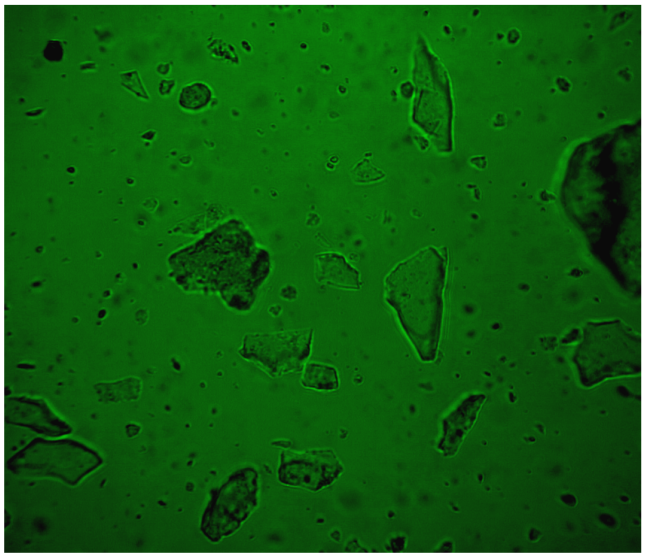

(a) Becke line outside fragments

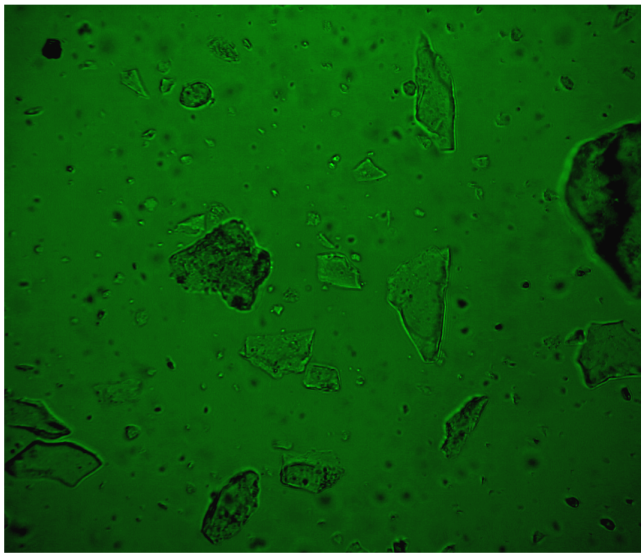

(b)

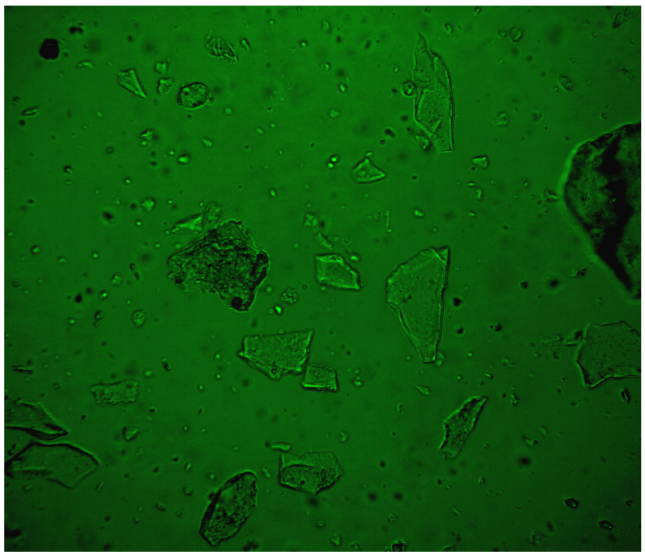

(c)

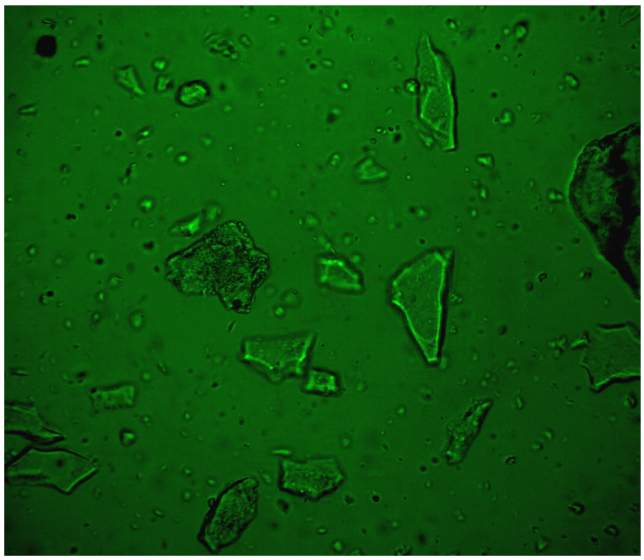

(d) Becke line inside fragments

liquids will typically determine that the particle refractive index lies between two liquids incremented by 0.01, or a near perfect match with a single liquid may be found. When the particle refractive index is found to lie between two liquids, it is appropriate to assign the refractive index of the particle to be at the midpoint unless a noticeable difference in particle contrast is observed in the two cases. For example if the particle refractive index is found to lie between 1.56 and 1.57 and both images have equal contrast then the value 1.565 should be assigned as the particle refractive index. If, however, the image in

Figure 5.2: Grímsvötn Ash in 1.65 refractive index liquid with 650 nm filter. From (a) to (b) the objective lens is raised and the Becke line is seen to move out ot the particles, indicating that the liquid has a higher refractive index than the fragments.

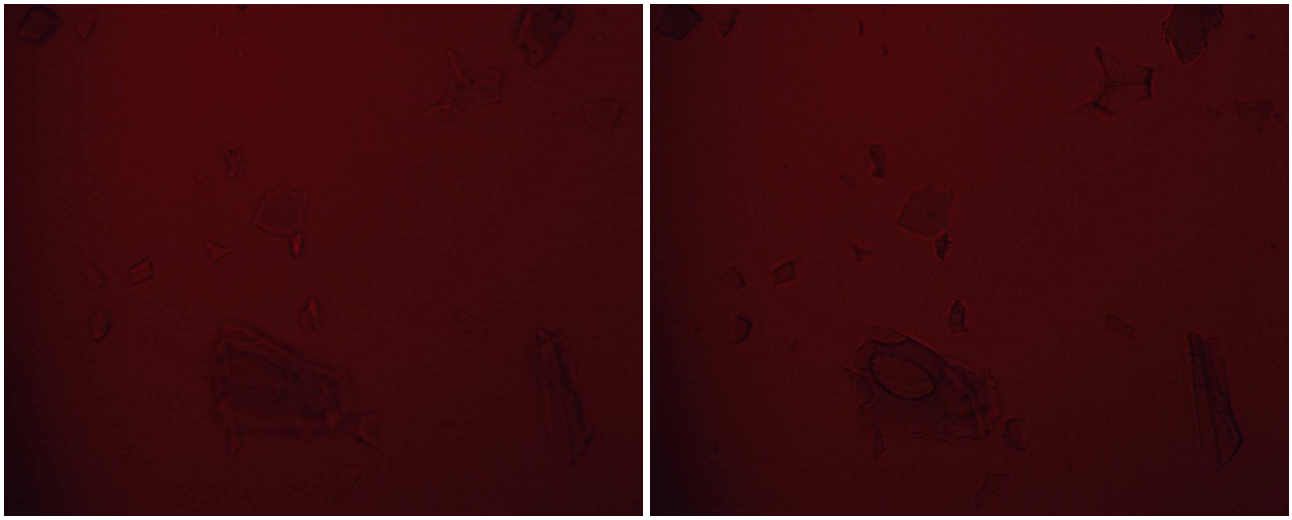

(a) Becke line inside fragments. **(b)** Becke line outside fragments.

Figure 5.3: Icelandic Ash in 1.60 refractive index liquid with 450 nm filter. From (a) to (b) the objctive lens is raised and the Becke line is seen to move out ot the particles, indicating that the liquid has a higher refractive index. Note that the human eye is less sensitive to contrast in the blue region of the visible.

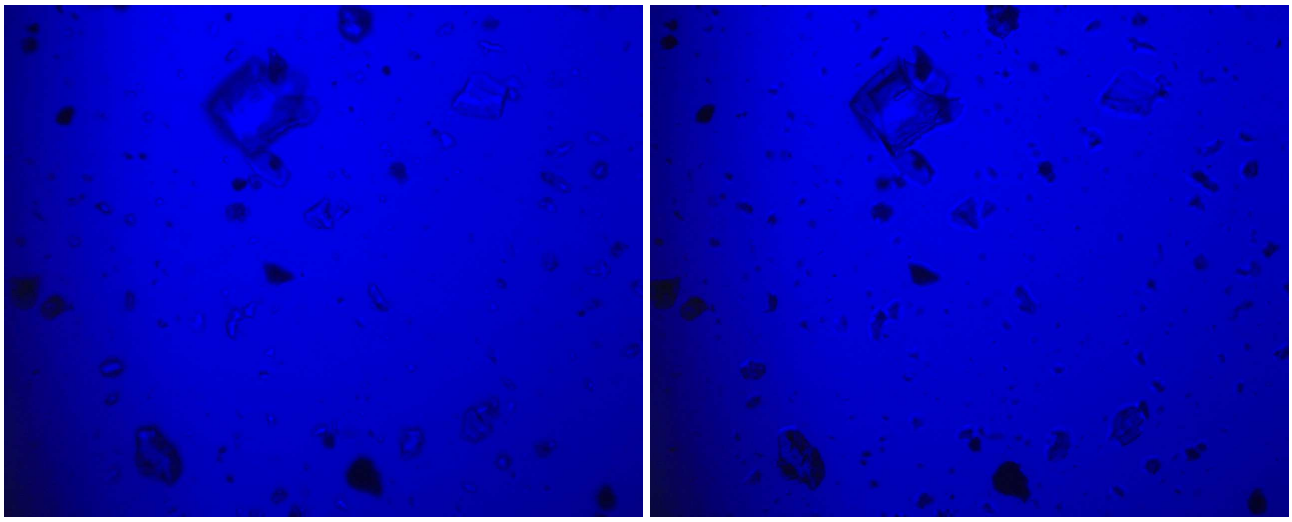

(a) Becke line inside fragments. **(b)** Becke line outside fragments.

the 1.56 liquid is noticeably fainter — indicating the particle refractive index lies closer to 1.56 — then it is appropriate to assign the refractive index as 1.5625.

- For cases where there is a noticeable degree of inhomogeneity with respect to particle refractive index in the sample, it is necessary to determine the Becke line displacement

for the majority of particles. Typically as the mean refractive index of particles approaches that of the liquid, an increasing minority of particles will have a Becke line displacement opposing that of the majority. It is typically possible to determine that the mean refractive index of particles lies between two liquids, as the direction of Becke line displacement of the majority of particles switches between the two. It may also be found that for one liquid the Becke line displacement of approximately 50% of particles in the field of view is in one direction, and 50% move in the opposite direction. In these cases it is typically found that there is a clear majority displacement in the two adjacent liquids, and thus the mean particle refractive index is assigned to be that of the liquid with 50/50 displacement.

5.3 Results and Analysis

5.3.1 Particle Size Range

It is important to specify precisely the range of particle sizes for which the Becke line measurements of refractive index apply. Specifically it is necessary to determine the smallest particle diameter for which the Becke line can be resolved.

Figure 5.4 shows images taken of a graticule using the 20x objective lens and in the same set up employed during the Becke line measurements. Image (a) is a full field of view image of the graticule, and similarly image (b) is a full field of view image of Cape Verde Dust fragments. In order to demonstrate the minimum particle size for which the Becke line is resolvable, (c) and (d) are identically cropped images of the graticule and Cape Verde Dust fragments respectively. By comparing these images it can be determined that the minimum particle diameter for which the Becke line can be resolved is $\sim 1\,\mu$m. Thus the Becke line refractive index measurements presented here apply for pariticles with diameters $\geq 1\,\mu$m.

5.3.2 Sample refractive index results and analysis

Table 5.1 shows the results for the mean refractive index of particles, n_p, with diameters $\geq 1\,\mu$m for various ash and dust samples. The results are given for the 3 wavelengths analysed: 450 nm, 546.1 nm and 650 nm. In addition, the table also includes an approximate estimate of the percentage SiO_2 content of the sample. This value was calculated based on the work done by *Kittleman* [1963] correlating the SiO_2 content of volcanic rock to its refractive index.

It can be seen from Table 5.1 that measurements have been made for a broad range of aerosol refractive indices, ranging from less than 1.505 up to 1.722 at 546.1 nm. The 'Rhyolite Ash Chaiten' sample was found to have a refractive index lower than that of the refractive index liquid available. This indicates that additional lower refractive index liquids need to be ordered for future Becke line measurements. The derived percentage SiO_2 content demonstrates that the volcanic ash samples tested span the 4 volcanic rock types — Basalt, Andesite, Dacite and Rhyolite.

The tests performed on the fine separated commercial sand sample were used as an independent check of the CSM refractometer results for scans on the same sample, as discussed in detail in §4.5.5.

Figure 5.4: Demonstration of the minimum resolvable Becke line particle size. Images (a) and (b) were taken with the 20x objective and show the full field of view. Images (c) and (d) have been cropped by identical factors: They demonstrate that the minimum particle size for which the Becke line is resolvable is approximately 1 μm.

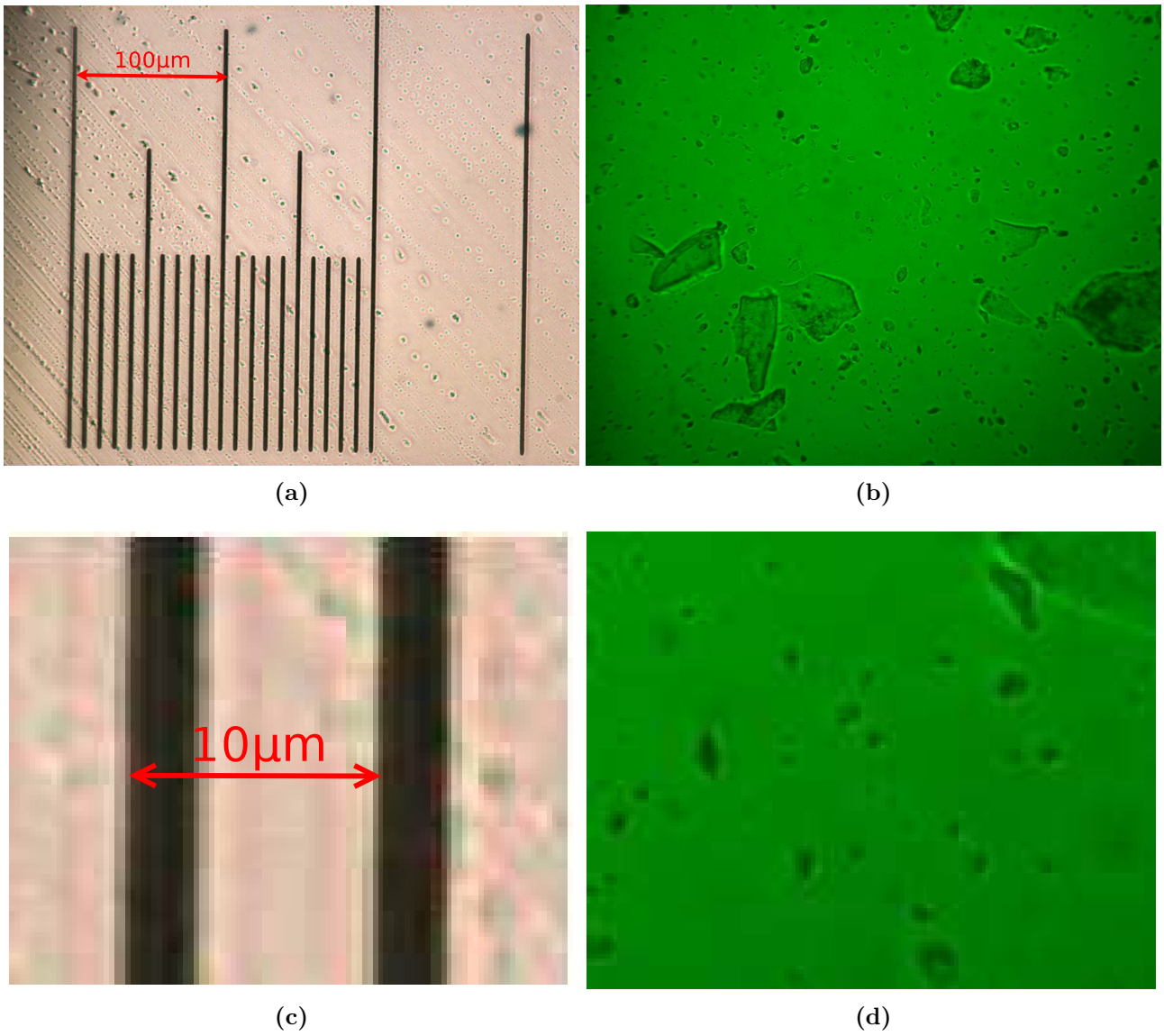

(a) **(b)**

(c) **(d)**

It can be seen from Table 5.1 that the refractive indices of the 3 'Eyjafjallajokull–May 2010 erup.' samples are very similar, and can not be distinguished given the uncertainty of ± 0.01. Each sample was collected at a slightly different location soon after the eruption. It can be seen that there is a distinguishable difference, given associated uncertainties, between the refractive index of the Eyjafjallajokull sample from the April eruptions compared to the 3 samples from the May eruptions. This indicates a compositional change in the volcanic ash with time. Such an observation is consistent with the detailed time-dependent compositional analysis of the Eyjafjallajokull fallout performed by *Sigmarsson et al.* [2011]. The derived approximate values for the SiO_2 content from the Becke line measurement are consistent with the values obtained

by *Sigmarsson et al.* [2011].

The ability to make inferences about composition from measurements of refractive index is useful in the case of volcanic ash samples because it allows one to relate back to volcanology and source geology of the eruption. This is also important for SPARCLE — if the device is able to infer refractive index in addition to particle size, then it would be possible to form size distributions for different compositional modes in a sample.

Table 5.1: Results for Becke line measurements of mean particle refractive index for various ash and dust samples. In addition an approximate estimate of the SiO_2 content is included for the volcanic ash samples based on the linear correlation found by *Kittleman* [1963].

Aerosol Sample	Mean Particle Refractive Index, $n_p(\lambda)$			Approximate SiO_2 content (percentage)
	$\lambda = 450.0\,\text{nm}$	$\lambda = 546.1\,\text{nm}$	$\lambda = 650.0\,\text{nm}$	
Cape Verde Dust	1.583 ± 0.01	1.572 ± 0.01	1.563 ± 0.01	
Mt Aso Volcanic Ash (1993 eruption)	1.577 ± 0.01	1.562 ± 0.01	1.553 ± 0.01	56 (Andesite)
Grímsvötn Volcanic Ash (collected 25/05/11 in Skaffafel)	1.629 ± 0.01	1.608 ± 0.01	1.597 ± 0.01	47 (Basalt)
Grímsvötn Volcanic Ash (collected 01/06/11 200 m from vent)	1.623 ± 0.01	1.608 ± 0.01	1.596 ± 0.01	47 (Basalt)
Eyjafjallajokull–April 2010 erup. (collected 17/04/10, 6 km from vent)	1.572 ± 0.01	1.562 ± 0.01	1.554 ± 0.01	60 (Andesite)
Eyjafjallajokull Tourist Sample (unverified origin)	1.554 ± 0.01	1.546 ± 0.01	1.548 ± 0.01	60 (Andesite)
Eyjafjallajokull–May 2010 erup. No.7 (collected 13/06/10)	1.554 ± 0.01	1.543 ± 0.01	1.536 ± 0.01	61 (Andesite)
Eyjafjallajokull–May 2010 erup. No.8 (collected 13/06/10)	1.554 ± 0.01	1.538 ± 0.01	1.536 ± 0.01	62 (Andesite)
Eyjafjallajokull–May 2010 erup. No.9 (collected 13/06/10)	1.560 ± 0.01	1.543 ± 0.01	1.541 ± 0.01	61 (Andesite)
Etna Ash (collected 27/12/02 near Zafferana)		1.600 ± 0.01		48 (Basalt)
Etna E2	1.605 ± 0.01	1.593 ± 0.01	1.582 ± 0.01	50 (Basalt)
Afar Boina BA1	1.521 ± 0.01	1.513 ± 0.01	1.507 ± 0.01	66 (Dacite)
Afar Boina BA2	1.516 ± 0.01	1.516 ± 0.01	1.519 ± 0.01	67 (Dacite)
JSC1A	1.617 ± 0.01	1.603 ± 0.01	1.592 ± 0.01	
Al_2O_3	1.747 ± 0.01	1.722 ± 0.01	1.705 ± 0.01	
Rhyolite Ash Chaiten	$< 1.516 \pm 0.01$	$< 1.505 \pm 0.01$	$< 1.499 \pm 0.01$	$> 70\,\%$ (Rhyolite)
Fine Separated Commercial Sand		1.566 ± 0.01	1.560 ± 0.01	

Chapter 6

Conclusions and future work

6.1 Conclusions

The refractomoeter results presented in §4.5 demonstrate that the apparatus is able to retrieve the refractive index of a homogeneous substance to a high level of accuracy, thus providing a check of apparatus performance independent of CSM theory. The results for the polystyrene latex test particles (§4.5.4) validate the use of CSM theory for the retrieval of aerosol optical properties for a spherical monodisperse sample from the reflectivity scan data. The polystyrene latex particles used where spherical and had a known monodisperse size distribution. As such they differ from a typical aerosol sample of interest to atmospheric physicists. The refractometer measurements made on the 'ash-like' commercial sand sample (§4.5.5) are promising and demonstrate that CSM (with a monodisperse assumption) can be used to retrieve physically sensible optical properties — the value retrieved for the particle refractive index agreed with the value obtained from Becke line measurements, to within propagated uncertainties.

The CSM refractomoter is sensitive to refractive index for particles with $a < 500\,\mathrm{nm}$ (as demonstrated by the analysis of §4.3), whereas the Becke line technique is limited by the resolving power of the microscope and so is valid for $a > 500\,\mathrm{nm}$ (§5.3.1). It is hoped that with future refractometer results for aerosol samples, the two techniques will provide comprehensive refractive index measurements with respect to particle size.

6.2 Plan for future work

6.2.1 Further work with the CSM refractometer

The refractometer CSM retrieval results for the 'ash-like' commercial sand sample are encouraging. The plan in the coming weeks is to apply the sedimentation technique to volcanic ash samples, and perform refractometer scans on the fine separated samples. Care will need to be taken because the volcanic ash samples available are limited in size, and a considerable mass of the bulk sample is required to produce sufficient fine material appropriate for the refractometer.

An additional area that needs consideration is the extension of the CSM retrieval to non-monodisperse size distributions. This work will be carried out in the coming weeks. Size distribution measurements will be made using an Aerodynamic Particle Sizer (APS) on the

fine separated volcanic ash sample (such measurements have already been made on the bulk samples), and this data will be utilised in the CSM retrieval of particle refractive index. The extension of CSM to paricle size distributions can be acheived by relatively simple alterations to equations 4.2 and 4.3 in §4.2, to a new form integrated over the size distribution [*Barrera et al.*, 2005]:

$$\alpha = \frac{-2\pi}{k_m^2 \cos(\theta_m)} \int_0^\infty \rho(a) S_a(0)\, \mathrm{d}a \tag{6.1}$$

$$\beta = \frac{-2\pi}{k_m^2 \cos(\theta_m)} \int_0^\infty \rho(a) S_{j,a}(\pi - 2\theta_m)\, \mathrm{d}a \tag{6.2}$$

The validation of the refractometer device and CSM retrieval presented in this report will form part of a paper on the development of the new technique. Future results derived from measurements of volcanic ash samples using the refractometer, and incorporating APS size distribution data, could then potentially form a second paper. The plan is to have at least one paper submitted by the end of the year, with the second paper following as soon as possible thereafter.

See Table 6.1 for a summary of the plan for future work on the CSM refractometer.

6.2.2 Work on SPARCLE

In the new year, following the completion of the CSM refractometer work, I will begin work on the further development of SPARCLE, an advanced Optical Particle Counter (OPC). The device has the potential to measure, on a particle by particle basis, both particle size and refractive index simultaneously — a unique concept in aerosol measurement. The measurements of refractive index already made as well as future measurements with the refractometer will therefore provide an invaluable check of results derived from SPARCLE. It is hoped the methods developed this year and the future work on SPARCLE will provide a comprehensive suite of techniques for the measurement of aerosol optical properties.

The device is in its its second phase of construction since the initial Stratospheric Aerosol Composition and Loading Experiment (SPARCLE) instrument was designed and developed by Dr Gareth Thomas in 2003. Following HEFCE funding in 2007 the device design was moved in order to make tropospheric aerosol measurements. Additionaly new design tools were developed by Dr Peters and Dr Andrew Smith to predict instrument performance.

The aim will be to overcome some of the issues that currently exist with the device, so that it is able to make size and refractive index measurements on a particle by particle basis. The device is currently limited by the digitisation noise of the electronics, rather than shot noise associated with the discretised nature of photons. Thus, the first area for work will be on increasing the gain of the electronic signal amplification, to ensure that the signal is limited by shot noise.

An additional area for work is improving the air flow controlling the flow of particles through the device's scattering chamber. In the current set up the flow must be continuously monitored and manual adjustments made to ensure the correct flow rate of particles is produced through the scattering chamber. Work will be carried out to switch to a closed loop flow set up, whereby the device uses an automatic feedback system to maintain the correct air flow through the device.

Once these modifications have been made, it will be necessary to test the device's performance using test particles with known physical properties. The ultimate aim is then to make measurements on aerosol samples, retrieving particle size and refractive index on a particle by particle basis. In this way integrated particle size and refractive index distributions can be measured for a wide range of aerosol samples.

See Table 6.1 for a summary of the plan for future work on SPARCLE.

Table 6.1: Summary of plan for future work, including estimated start and finish dates for each task.

Task Description	**Estimated Start Date**	**Estimated Finish Date**
Modifying CSM forward model to incorporate APS size distribution data.	Week 1 November 2012	Week 2 November 2012
Perform CSM refractometer scans on ash samples.	Week 1 November 2012	Week 4 November 2012
Obtain APS size distribution data for fine separated ash samples.	Week 2 November 2012	Week 4 November 2012
Write CSM technique and validation paper.	Week 3 November 2012	Week 2 December 2012. Target submission: End of 2012
Work on SPARCLE.	January 2013	January 2015
Improve signal to noise ratio, by increasing electronic gain.	January 2013	March 2013
Set up closed loop flow.	March 2013	May 2013
Perform experiments using test particles.	May 2013	August 2013
Optimise SPARCLE retrieval.	May 2013	November 2013
Use SPARCLE to measure real aerosol samples.	August 2013	March 2014
Data analysis and reduction.	April 2014	May 2014
Write up thesis.	June 2014	September 2015

6.3 Transferable skills

- **Presentation skills:** I presented a 15 minute talk on my work and the measurements I have made at a meeting on volcanic ash in the department. I received positive feedback about the talk.
- **Latex document preparation skills:** Writing this report has improved my document preparation and presentation skills. I have also learnt how to effectively keep track of my references using Bibtex.

- **IDL programming:** Since working in the department I have become familiar with programming in the language.

Bibliography

Albrecht, B. A., Aerosols, cloud microphysics, and fractional cloudiness, *Science*, *245*, 1989.

Barrera, R. G., and A. García-Valenzuela-Valenzuela, Coherent reflectance in a system of random mie scatters and its relation to the effective-medium approach, *Journal of the Optical Society of America*, *20*, 2003.

Barrera, R. G., A. García-Valenzuela-Valenzuela, C. Sanchez-Perez, A. Reyes-Coronado, and E. R. Mendez, Coherent reflection of light from a turbid suspension of particles in an internal reflection configuration: Theory versus experiment, *Optics Express*, *18*, 2005.

Bianco, R., and J. T. Hynes, Heterogeneous reactions important in atmospheric ozone depletion: A theoretical perspective, *Accounts of Chemical Research*, *39*, 2006.

Bohnen, C. F., Applicability of effective medium theories to problems of scattering and absorption by non-homogeneous atmospheric particles, *Journal of Atmospheric Sciences*, *43*, 468, 1986.

Bohren, C. F., and D. R. Huffman, *Absorption and Scattering of Light by Small Particles*, John Wiley & Sons, 1983.

Bruggeman, D. A. G., Berechnung verschiedener physikalicher konstanten von heterogenen substanzen. i. dielektrizitätkonstanten und leirfähigkeiten der mischkörper aus isotropen substanzen, *Annals of Physics (Leipzig)*, *24*, 636–679, 1935.

Garnett, J. C. M., Colours in metal glasses and in metallic films, *Philosophical Transactions of the Royal Society of London*, *203*, 385–420, 1904.

Hale, G. M., and M. R. Querry, Optical constants of water in the 200 nm to 200 μm wavelength region, *Applied Optics*, *12*, 1973.

Hapke, B., *Theory of Reflectance and Emittance Spectroscopy, Topics in Remote Sensing*, Cambridge University Press, 1993.

Kasarova et al., S. N., Analysis of the dispersion of optical plastic materials, *Optical Materials*, *29*, 2007.

Kittleman, L., Glass-bead silica determination for a suite of volcanic rocks from the owyee plateau, oregon, *Geological Society of America Bulletin*, *73*, 1963.

Kuga, Y., D. Rice, and R. D. West, Propagation constant and the velocity of the coherent wave in a dense strongly scattering medium, *IEEE Transactions on Antennas and Propagation*, *44*, 326–332, 1996.

Loiko, V. A., V. P. Dick, and A. P. Ivanov, Features in coherent transmittance of a monolayer of particles, *Journal of the Optical Society of America*, *A 17*, 2040–2045, 2000.

Meeten, G. H., and A. N. North, Refractive index measurement of absorbing and turbid fluids by reflection near the critical angle, *Measurement Science and Technology*, *6*, 214, 1995.

Mohammadi, M., Colloidal refractometry: meaning and measurement of refractive index for dispersions; the science that time forgot, *Advances in Colloid and Interface Science*, *62*, 1995.

Ramaswamy, V., et al., Stratospheric temperature trends: Observations and model simulations, *Reviews of Geophysics*, *39*, 2001.

Rayleigh, J. W. S., On the transmission of light through an atmosphere containing small particles in suspension, and on the origin of the blue of the sky, 1899.

Rosenfeld, D., Aerosol-cloud interactions control of earth radiation and latent heat release budgets, *Space Science Review*, *125*, 2006.

Sigmarsson, O., et al., Remobilization of silicic intrusion by mafic magmas during the 2010 eyjafjallajkull eruption, *Solid Earth*, *2*, 2011.

Solomon, S., D. Qin, M. Manning, Z. Chen, M. Marquis, K. B. Averyt, M. Tignor, and H. L. Miler, *Contribution of Working Group I to the Fourth Assessment Report of the Intergovernmental Panel on Climate Change, 2007*, Combridge University Press, 2007.

Sumitra Optical glass Inc., Sumitra optical glass data sheet, `http://refractiveindex.info/`, 2012.

Tsang, L., and J. A. Kong, Multiple scattering of electromagnetic waves by random distribution of discrete scatterers with coherent potential and quantum mechanical formalism, *Journal of Applied Physics*, *51*, 3465–3485, 1980.

Tsang, L., and J. A. Kong, Effective propagation constants for coherent electromagnetic waves propagating in media embedded with dielectric scatters, *Journal of Applied Physics*, *53*, 7162, 1982.

Twomey, S., The influence of pollution on the shortwave albedo of clouds, *Journal of Atmospheric Sciences*, 1977.

van der Hulst, H. C., *Light Scattering by Small Particles*, Dover Publications, New York, 1957.

Xiaoyan, M., Q. L. Jun, R. S. Brock, K. M. Jacobs, P. Yang, and X. Hu, Determination of complex refractive index of polystyrene microspheres from 370 to 1610 nm, *Physics in medicine and biology*, *48*, 2003.